

Elsevier Editorial System(tm) for  
Sedimentary Geology  
Manuscript Draft

Manuscript Number: SEDGEO7677R1

Title: Characteristics and emplacement mechanisms of the Coranzulí ignimbrites (Central Andes)

Article Type: Research Paper

Keywords: Coranzulí; Central Andes; Puna; crystal-rich ignimbrites; Pyroclastic Density Current; Altiplano-Puna Volcanic Complex

Corresponding Author: Dr. Silvina Guzman,

Corresponding Author's Institution:

First Author: Silvina Guzman

Order of Authors: Silvina Guzman; Domenico M Doronzo; Joan Martí; Raul E Seggiaro

Abstract: We present a detailed stratigraphy of the Coranzulí caldera-forming deposits. This caldera, located in the Altiplano-Puna Volcanic Complex (Central Andes), generated four ignimbrite deposits with similar field characteristics and facies that differ from each other in, above all, the nature of the lithic fragments they contain. Three different lithofacies (fine-grained cross-stratified facies, massive lithic breccia facies and massive ignimbrite facies) are found in all the ignimbrite deposits, which occasionally also contain a lenticular lithic-rich facies and/or a pumice-rich facies. These field characteristics and, in particular, local deposit thicknesses were used to develop a theoretical model of the dynamics and emplacement mode of the Coranzulí pyroclastic flows. Our results show that these ignimbrites were emplaced by dense pyroclastic density currents subjected to high accumulation rates and velocities, thereby indicating rapid en masse emplacement that was also influenced by local paleotopography as deduced from facies analysis.

Research Data Related to this Submission

-----  
There are no linked research data sets for this submission. The following reason is given:  
Data will be made available on request

29 APVC (latitude 21–24°S, the Andes) produced more than 15,000 km<sup>3</sup> of crystal-rich dacitic  
30 ignimbrites (e.g., de Silva et al., 2015) originating mostly from calderas. The intense volcanism of this  
31 area has been related to the existence of a low-velocity zone at mid-crustal levels known as the  
32 Altiplano-Puna Magma Body (e.g., Chmielowski et al., 1999).

33 The APVC contains at least eight calderas but the sources of many of its ignimbrite units are still  
34 unknown or buried, as is the case of the Abra Granada Ignimbrite (Caffe et al., 2008). The caldera  
35 complexes in the APVC (Fig. 1) with the greatest volumes (800-2500 km<sup>3</sup>) are La Pacana, Cerro  
36 Guacha I, Cerro Guacha II, Pastos Grandes, Kapina and Vilama (de Silva, 1989; Lindsay et al., 2001a;  
37 Soler et al., 2007; Salisbury et al., 2011; Iriarte, 2012; Grocke et al., 2017). The calderas of Cerro  
38 Panizos and Coranzulí (each about 650 km<sup>3</sup> and 6.5-7 Ma) to the east have slightly smaller volumes  
39 and are peraluminous (Seggiaro et al., 1987, 2019; Ort, 1993).

40 Studies of the calderas in the APVC have to date mainly focused on their petrologic  
41 characteristics, chronology, volume estimations, the definition of their rims and structural controls, as  
42 well as the type of collapses (e.g., de Silva, 1989; Seggiaro, 1994; Ort et al., 1996; Lindsay et al.,  
43 2001a,b; Soler et al., 2007; Salisbury et al., 2011; Grocke et al., 2017; Seggiaro et al., 2019).  
44 Consequently, less attention has been paid to their stratigraphy and the modes of emplacement and  
45 deposition of the caldera-forming products, although a few studies of these calderas to varying degrees  
46 of detail do exist (e.g., Seggiaro et al., 1987; Ort, 1993; Lindsay et al., 2001a; Soler et al., 2007).

47 To further knowledge of the APVC ignimbrite deposits and characterise the emplacement and  
48 depositional mechanisms of these large-volume ignimbrites, we concentrated our study on the caldera-  
49 forming products originating from the Coranzulí caldera (Seggiaro et al., 1987, 2019). Our aim was to  
50 develop a theoretical model of the dynamics of the Coranzulí pyroclastic flows that furthers our  
51 knowledge of the behaviour of such large pyroclastic density currents (PDCs) and their depositional  
52 mechanisms.

53 Pyroclastic density currents and their deposits are generally studied using a number of  
54 different approaches (fieldwork, experimental and numerical studies) and with a variety of objectives  
55 in mind (emplacement and hazard) (Roche et al., 2013; Sulpizio et al., 2014; Neri et al., 2015; Dufek,  
56 2016). In particular, dense PDCs emplacing ignimbrites have been studied by integrating theoretical,

57 stratigraphic, sedimentological, petrological, paleomagnetic and, more recently, experimental work  
58 (e.g., Sparks et al., 1978; Cas and Wright, 1987; Druitt, 1998; Branney and Kokelaar, 2002; Ort et al.,  
59 2013; Rowley et al., 2014; Roche, 2015). It is thought that dense PDCs emplacing ignimbrites are  
60 thermally conservative flows (McClelland et al., 2004; Lesti et al., 2011; Cas et al., 2011; Sulpizio et  
61 al., 2014; Giordano and Doronzo, 2017; Platzman et al., 2020). They can move whilst retaining  
62 temperature for several kilometres under the action of sustained pyroclastic fountaining with high  
63 mass eruption rates (MERs) during caldera collapse (Martí et al., 2009; Cas et al., 2011; Willcock et  
64 al., 2013; Roche et al., 2016; Trolese et al., 2017) or under the action of flow channelization (Doronzo  
65 et al., 2016; Martí et al., 2017, 2019; Pensa et al., 2019).

66 Our current understanding of the emplacement mechanisms of thermally conservative flows to  
67 form ignimbrites is still not fully clear due to four principal physical complexities: (i) the transmission  
68 of inertia from a low pyroclastic fountain to a dense PDC; (ii) the time-dependent evolution of pore  
69 pressure within the dense PDC; (iii) the size of the dense PDC (erupted volume versus areal extent of  
70 the PDC); and (iv) the emplacement mechanisms and temperature retention of ignimbrites  
71 (McClelland et al., 2004; Lesti et al., 2011; Cas et al., 2011; Doronzo, 2012; Roche, 2012; Roche et  
72 al., 2016; Sulpizio et al., 2014; Dufek, 2016; Dellino et al., 2019).

73 In order to accomplish such objective, we used previous (Seggiaro et al., 1987, 2019) and new  
74 field data of the four ignimbrite units that were emplaced during the formation of the Coranzulí  
75 Caldera, mainly concentrating on their lithological and sedimentological characteristics, as well as  
76 their stratigraphic relationships and facies variations. Using this information, we present here a  
77 theoretical depositional model for these deposits aimed at simplifying the above-mentioned  
78 complexities. This model follows reverse engineering and inverts the deposit thicknesses to calculate  
79 accumulation rates and velocities, which can be combined with field data to interpret flow  
80 emplacement, local inertia loss and interaction with topography. The accumulation rates of a  
81 pyroclastic flow deposit or, in general, of a sedimentary deposit are probably the best parameter for  
82 denoting the transition from flow to deposit given the need for a framework in which flow structure  
83 and deposit structure are the same (e.g., Roche, 2015). Hence, we kept the model as simple as possible  
84 and closely linked to field characteristics.

85

## 86 **2. Geological setting of the Coranzulí caldera**

87           The Coranzulí Caldera (Fig. 2) lies on the Altiplano-Puna Plateau, within the Central Andes  
88 Volcanic Zone (18-28°S segment of the Andes) (e.g., Harmon et al., 1984; Stern, 2004). It is located  
89 in at ca. 140 km from the present volcanic arc, in the back-arc region. The present-day uplifted  
90 topography of the Altiplano-Puna Plateau has been attributed to tectonic shortening induced by the  
91 subducting Nazca Plate and, also to magmatic addition (e.g., Isacks, 1988; Allmendinger and  
92 Gubbels, 1996; Kay et al., 1999; Oncken et al., 2006).

93           The Altiplano-Puna Plateau is structurally controlled by several sets of fault systems oriented  
94 N-S to NNE-SSW, NW-SE and NE-SW ( Salfity, 1985; Riller and Oncken, 2003) and the volcanic  
95 centres they contain are aligned along these fault systems ( Mon, 1979; Salfity, 1985; Marrett and  
96 Emerman, 1992; Riller et al., 2001; Richards and Villeneuve, 2002; Trumbull et al., 2006; Guzmán et  
97 al., 2014; Tibaldi et al., 2017). This is the case of the Coranzulí Caldera, which is located at the  
98 intersection of N-S, NW-SE and NE-SW fault systems (Seggiaro et al., 2014, 2019).

99           The Coranzulí Caldera (23° 00'S- 66° 15' W) is located in the Northern Puna (ca. 24–21.5  
100 °S). Its basement consists of Paleozoic and Mesozoic granitoids and marine Ordovician rocks  
101 interbedded with volcanic and subvolcanic successions (Coira, 1973). Although no high-grade  
102 metamorphic pre-Ordovician outcrops exist in the Northern Puna, the presence of accessory lithic  
103 fragments of sillimanitic gneisses within the Coranzulí ignimbrites points to the presence of such a  
104 basement beneath the Ordovician sediments (Seggiaro, 1994). The pre-caldera sedimentary  
105 successions are composed of Cretaceous syn-rift and Paleogene post-rift deposits belonging to  
106 carbonatic and clastic deposits of the Salta Group and of Eocene–Miocene volcano-sedimentary  
107 deposits (See Fig. 2 in Seggiaro et al., 2019).

108           Pre-caldera Cenozoic volcanic activity in the Coranzulí area is represented by sandstones,  
109 pyroclastic successions and reworked volcanic material from the Middle Miocene (Seggiaro and  
110 Aniel, 1989). To the east of Coranzulí Caldera there are deposits of 7.2–8.4 Ma belonging to the  
111 Rachaite stratovolcano of andesitic–dacitic composition (Coira et al., 1993; Kay et al., 2010, and

112 references therein). To the southwest outcrops the Morro Grande Ignimbrite, consisting of massive  
113 and brecciated pyroclastic deposits of similar composition to those of the Coranzulí ignimbrites  
114 (López et al., 2016) covered by lacustrine deposits interbedded with massive and stratified pyroclastic  
115 deposits of  $6.99 \pm 0.18$  Ma (Alonso, 1986). The Coranzulí ignimbrites overlie these successions (see  
116 Fig. 2 in Seggiaro et al., 2019).

117

### 118 **3. Methodology**

119

120 In addition to the previous stratigraphic data available on the Coranzulí ignimbrites, we  
121 constructed 20 new stratigraphic logs chosen on the basis of their accessibility, quality of exposure  
122 and degree of preservation (Fig. 3). In each stratigraphic log we recorded lithological and  
123 sedimentological data, including component analysis at macroscopic and microscopic scales, grain-  
124 size estimates for pumices and lithics, characterisations of basal and top contacts for each ignimbrite  
125 unit, and the thickness of each deposit. Previous and new stratigraphic data were combined in order to  
126 establish the stratigraphic correlations and facies variations of these deposits. We also measured the  
127 five largest pumice and lithic fragments (minimum and most frequent sizes) in each ignimbrite unit, as  
128 well as the maximum and minimum axes of pumice/fiamme to determine their aspect ratios. Other  
129 standard descriptions such as colour, induration degree, size of the matrix and the recognition of  
130 textures and fabrics were also noted.

131

### 132 **4. Results**

133 As it was already indicated by Seggiaro et al. (1987, 2019), the stratigraphic succession of the  
134 Coranzulí Caldera is composed of four different ignimbrite units. Seggiaro et al. (2019) suggested that  
135 these ignimbrites derived from four different PDCs each of which originated from a specific sector of  
136 the ring fault at a particular stage of the caldera collapse process. Our field revision confirms this  
137 stratigraphy and the fact that each ignimbrite units was emplaced from a different sector of the caldera.

138 The base of each ignimbrite is marked by lithic breccias at proximal distances ( $<5$  km), while  
139 at medial distances from the caldera (5–15 km) contacts are identified by fine-grained ash layers.

140 However, in some outcrops the contact between ignimbrites is not that evident and they can be only  
141 distinguished by the nature and proportion of the lithic fragments they contain. The contacts between  
142 the ignimbrites can be erosional or gradational depending on the observation point, and internally they  
143 may show variations in grain size and the percentage of juvenile and lithic components, and variations  
144 in primary bedforms. All the ignimbrite units exhibit the same types of facies, e.g., fine-grained cross-  
145 stratified facies, massive lithic breccia facies and massive ignimbrite facies, which form the main body  
146 of the deposits; occasionally, they may also contain a lenticular lithic-rich facies and/or a pumice-rich  
147 facies. The characteristics of each facies are very similar in each ignimbrite unit despite certain  
148 differences in the nature of the lithic fragments, the size and degree of flattening of the pumice clasts,  
149 the degree of welding and the thickness of each one.

150         Near the northern edge of the caldera rim the base of the unexposed pre-caldera deposits  
151 consists of a ~10-m-thick massive indurated monolithologic breccia (Fig. 4a, b) with a matrix of fine  
152 ash containing 50–70% volume of subangular lithic fragments of dacitic lavas ranging in size up to  
153 30–40 cm in diameter (Fig 4b). This massive and monolithologic volcanic breccia contains no pumice  
154 but does contain some vitrophyres with perlitic alteration.

155

#### 156 *4.1 Ignimbrite unit 1*

157         This ignimbrite flow unit was emplaced north- and northwestwards but only towards the north  
158 of the caldera the base of this unit is visible. The average thickness of the ignimbrite is 50 m and the  
159 flows that fed this ignimbrite travelled for at least 28 km from the caldera rim.

160         The base of this unit is formed by a 4–8 m-thick, yellow–greenish fine-grained cross-stratified  
161 facies, which overlies the pre-caldera monolithologic volcanic breccia (see log 1 in Fig. 3a). Its  
162 internal structures consist of low-angle cross-stratified beds (Fig. 4 a,c,d) with internal normal grading  
163 in some sets. They are composed of quartz, plagioclase and biotite crystals and crystal fragments and  
164 rounded, well-sorted, ash pumice grains, and are rich in small lithic fragments of dacitic lavas and  
165 Ordovician metapelites, as well as in small fine lapilli (~ 0.2–0.5 cm) white pumice fragments. Some  
166 layers (up to 50-cm thick) within this succession form lenticular lithic-rich facies (lensl; Figs. 3a, 4d),

167 in which rounded-to-subrounded lithic fragments of Ordovician pelites and dacitic lavas of up to 8 cm  
168 in diameter are concentrated in an ashy/fine lapilli matrix.

169 The fine-grained cross-stratified facies is covered by a massive lithic breccia facies (Figs. 3a,  
170 4a,e) (see log 1 in Fig. 3a) with a maximum thickness of 5 m. The pumice are white, about 25 vol. %,   
171 (<5 cm in diameter), while the subangular lithic fragments (~40%) consist of dacitic lavas (up to 35–  
172 50 cm in diameter) and minor, usually very small (~0.8 cm) Ordovician metapelitic fragments (log 1  
173 in Fig. 3a). Dense juvenile fragments (~3 vol. %) are rounded with a maximum size of 10 cm.

174 The massive ignimbrite facies (see log 1 in Fig 3a) is only exposed in a few places, probably  
175 because it has been covered by other younger ignimbrite units (unit 2, 3 or 4). It is grey and mostly  
176 indurated; its matrix consists of fine-to-medium ash and crystal fragments of bipyramidal quartz  
177 (translucent and pink), biotite and feldspars. Its degree of welding varies laterally and vertically, from  
178 low to moderate. The upper sections are welded and have columnar jointing. Its lithic content is low  
179 (1–3 vol. %) and decreases upwards and in distal facies and consists predominantly of dacitic lavas  
180 (log 1 in Fig. 3a) with maximum sizes of 14 cm (but usually <3 cm). The pumice content is variable,  
181 from 10–20 vol. %, and of variable sizes (usually <1 cm), white-to-yellowish or -black when they are  
182 welded, with maximum sizes of 12 cm. Dense juvenile fragments are observed in all sections at a  
183 proportion of about 1 vol. % with a diameter of <4 cm.

184

#### 185 *4.2 Ignimbrite unit 2*

186 The base of Unit 2 is characterised by a massive lithic breccia facies lying in some areas close  
187 to the caldera (see log 2 in Fig. 3a), although in other proximal and medial sections it has a stratified  
188 indurated ash layer (fine-grained cross-stratified facies) (see Seggiaro et al., 2019). The main body of  
189 the unit corresponds to a massive ignimbrite facies showing lithic-rich lenses (lenticular lithic-rich  
190 facies) in distal locations. The maximum outflow distance is 45 km.

191 This ignimbrite unit (see Figs. 2, 3) was deposited radially from the caldera (Seggiaro et al.,  
192 2019) but maximum thicknesses of 200 m are present to the east (see log 5 in Fig. 3b). In proximal  
193 areas its base corresponds to a massive lithic breccia facies, highly indurated and about 5-m thick to  
194 the north of the caldera (see log 2 in Fig. 3a). Within this breccia, the pumice are white, about 15 vol.

195 % (<5 cm but usually small, around 0.5 cm), while the lithic fragments (~20 –25 vol. %) are  
196 subangular. The main types of lithic fragments are Ordovician metapelites and quartzites (<27-cm  
197 long), whereas the dacites are subordinate. Dense juvenile fragments (~3 vol. %) reach maximum  
198 sizes of 4 cm. This massive lithic breccia facies may vary laterally (see log 3 in Fig. 3a) and develops  
199 diffuse stratification where pumice are larger (15 cm) and more abundant (30 vol. %), and lithic  
200 fragments are smaller and less abundant. At medial distances from the caldera the base of this  
201 ignimbrite unit corresponds to the fine-grained cross-stratified facies followed by the massive  
202 ignimbrite facies (see Fig. 3 in Seggiaro et al., 2019).

203         This massive ignimbrite facies forms the main body of the ignimbrite and is pink-to-grey in  
204 colour, with a degree of welding that varies vertically and laterally from low to high. Its matrix  
205 consists of medium-to-coarse ash and crystal fragments of pink and crystalline quartz (frequently  
206 forming bipyramidal grains), biotite and feldspars. Towards the east this ignimbrite unit is highly  
207 welded at proximal and medial distances, with fiamme aspect ratios of up to 14:1, whereas more  
208 distally (>15 km) there is only a very low degree of welding (fiamme aspect ratios of 2:1), albeit it is  
209 still indurated. The greatest amount of welding is to the north, towards the surface, and more distally,  
210 and has aspect ratios of 8:1. Pumice fragments are white-to-yellowish in colour in poorly welded  
211 sectors but form black (Fig. 5a) and pink fiamme (Fig. 5b) in welded sectors. The concentration of  
212 pumice clasts is highly variable both vertically and laterally; in proximal areas their content lies in the  
213 range 5–25 vol. % but they are usually more abundant towards the top of the succession. More  
214 distally, their content also varies greatly (5–30 vol. %). Except for the outcrops to the north, where  
215 well-defined fiamme (<16-cm long) are visible, all other distal exposures are non-welded, with white-  
216 to-yellow rounded pumice up to 10 cm in length and rich in crystal fragments. The largest pumice are  
217 found at intermediate distances from the caldera, where they reach up to 21 cm in diameter. The most  
218 common pumice size in both proximal and distal facies is 0.5–3 cm.

219         Lithic fragments are scarce, usually <1 vol. % but occasionally up to 7 vol. % (exceptionally  
220 they reach 25 vol. %), angular, predominantly composed of Ordovician metapelites and quartzites (see  
221 Fig. 3) and, to a much lesser extent, dacitic lava fragments. In sections to the east of the caldera there  
222 is an increase in dacitic lithic fragments towards the upper part of the deposit; however, in all cases

223 lithics from the Ordovician basement are the most abundant. Lithic fragments are usually small (0.5–4  
224 cm), although fragments measuring 16–18 cm are present in distal facies and proximal upper facies.  
225 Dense juvenile fragments are observed in all sections and are about 1–3 vol. %, with sizes of up to  
226 16.5 cm.

227 This lenticular lithic-rich facies is observed in distal zones and represents a transition to the  
228 massive ignimbrite facies in which it is hosted (Fig. 6a). This facies can be seen at the front of the  
229 flow unit (see log 14 in Fig. 3c) at approximately 18 km northwest of the caldera rim (see Fig. 2),  
230 where it is up to 2 m thick. The matrix is composed of coarse ash with a lithic content of about 40 vol.  
231 %, most of which consists of subangular (Fig. 6b) quartzites with a maximum clast size of 30 cm.

232

#### 233 *4.3. Ignimbrite unit 3*

234 This unit has a basal massive lithic breccia facies to the northwest of the caldera (see Casa  
235 Blanca log, Fig. 4 in Seggiaro et al., 2019) but is composed mainly of a massive ignimbrite facies with  
236 lenticular lithic-rich facies in proximal settings and a pumice-rich facies in the uppermost and  
237 proximal part of the deposit. Its average thickness is 40 m and its most distal outcrops are 37 km from  
238 the caldera rim. The basal massive lithic breccia facies attains a maximum thickness of 6 m and  
239 consists mainly of dense co-magmatic lithic fragments (up to 80 cm in diameter) and variable amounts  
240 of Ordovician sedimentary rocks, dacitic lavas and metamorphic lithics (gneiss) (Fig. 6c). As in the  
241 previous ignimbrite units, at medial distances the base of this third ignimbrite unit corresponds to an  
242 indurated ash layer visible in the Abra Grande log (Fig. 4 in Seggiaro et al., 2019).

243 The massive ignimbrite facies is light-to-dark grey or -pink due to surface alteration (Fig. 6d).  
244 Welding varies from low to high, being the most welded parts located towards the top of the deposit.  
245 The ignimbrite matrix consists of medium-to-coarse ash and crystal fragments of quartz (pink and  
246 crystalline), biotite and feldspars. Pumice fragments are white to yellow and rounded in non-welded  
247 facies; on the other hand, black and pink fiamme are found in the welded facies. Pumice content is  
248 variable (10–25 vol. %) but usually high (20–25 vol. %); pumice can be up to 17 cm in diameter,  
249 although the commonest sizes are 2–3 cm. This ignimbrite is poor in lithic fragments, usually <1 vol.  
250 %, and are mainly small (0.5–2 cm), reaching a maximum size of 26 cm in diameter in proximal and

251 basal zones. Lithic fragments are of the same type as those found in the massive lithic breccia,  
252 although small amounts of small-sized porphyritic dacites and Cenozoic red pelites and sandstones are  
253 also present. Rounded, dense juvenile grey lithic fragments represent 1–3 vol. % and are up to 25 cm  
254 in diameter.

255 A massive pumice-rich ignimbrite facies can be distinguished at proximal sites (see Seggiaro  
256 et al., 2019), where up to 25 vol. % of rounded pumices are concentrated towards the upper levels of  
257 the deposit. This facies has up to 3 vol. % of dense grey juvenile fragments that are <14 cm in  
258 diameter. Pumices are white-to-yellow, crystal-rich (30–60%) and usually subrounded and small (0.5–  
259 3 cm), even though larger fragments, frequently recognised as *fiamme*, can reach 18 cm in diameter.  
260 Fragments of dense juvenile fragments are ubiquitous, subrounded, up to 25 cm in diameter, with  
261 content <1–3% in volume.

262 Additionally, lenticular lithic-rich facies are observed at proximal facies in transition to the  
263 massive ignimbrite facies that host them. The main lithic type in this lenticular facies is dacitic lava  
264 (see Norte de Coranzulí log Fig 4 in Seggiaro et al., 2019).

265

#### 266 *4.4. Ignimbrite unit 4*

267 The fourth ignimbrite unit is located to the south of the caldera and travelled 18 km from the  
268 caldera rim. It has at its base a pink massive lithic breccia facies, ~ 8 m thick, that contains ~15–30  
269 vol. % of crystal-rich white pumice; its upper portion is highly indurated. It is characterised by the  
270 presence of blocks of dacitic ignimbrites (Fig. 7h) up to 50 cm in diameter, and minor sedimentary  
271 Ordovician lithics, dacitic lavas and a few metamorphic and granitoid fragments. Dense grey juvenile  
272 fragments up to 10 cm in diameter are also visible in this facies. The breccia is overlain by the massive  
273 ignimbrite facies, which in very proximal outcrops (log 15 in Fig. 3d) near the caldera rim have an  
274 interbedded fine-grained cross-stratified facies (Figs. 7 a-c). The latter forms individual layers of less  
275 than 2 m in thickness, each interbedded with the massive ignimbrite facies, which exhibit cross (Fig.  
276 7a) and planar (Fig. 7b) stratification and contain abundant pumice fragments and dense juvenile lithic  
277 fragments. In this facies, levels of concentrations of pumice (up to 50 vol. %) are common where the  
278 matrix presents vapour-phase alteration, probably due to the release of gases from the pumice

279 fragments during cooling. These layers, being originally more porous are hence more prone to vapour-  
280 phase alteration (Smith, 1960) are harder and darker than the unaltered layers (see Fig. 7d). Dense  
281 grey juvenile fragments are up to 30 cm in diameter in this succession. No other lithic fragments are  
282 present within this sequence of alternating stratified and massive facies.

283         The massive ignimbrite facies is grey-to-pink in colour and its matrix consists of medium  
284 grained ash and crystal fragments of quartz, biotite and feldspars. The degree of welding is variable,  
285 being greater in proximal and upper sections where columnar jointing is frequent (Figs. 7e) but only  
286 slightly welded-to-non-welded in distal outcrops. The pumice content is variable but is usually above  
287 20 vol. %, with some concentration levels of up to 50 vol. % (pumice-rich massive ignimbrite facies;  
288 see log 17 in Fig. 3d). The pumice are white and crystal-rich and rounded-to-subrounded when the  
289 ignimbrite is non-welded (Fig. 5c) but contain grey-to-black fiamme (Fig. 5d) when welded. Although  
290 most pumices are small (1–2 cm), maximum sizes vary from 8 to 18 cm, with the largest fragments  
291 visible at medial and distal distances from the caldera rim. This facies is lithic-poor (<1%) and usually  
292 has small fragments (0.5–1 cm with maximum sizes of <4 cm) of Ordovician pelites and quartzites,  
293 dacitic lavas, metamorphic fragments and Cenozoic red pelites and dacitic ignimbrites. Dense juvenile  
294 fragments (Fig. 5c) are <3 vol. %, and are up to 30 cm in diameter in proximal facies, 25 cm in medial  
295 facies, but smaller in distal facies.

296         The pumice-rich massive ignimbrite facies is found in proximal and distal areas (Fig. 7g) at  
297 about 18 km from the caldera rim. Pumices represent up to 50 vol. %, vary in size (0.5–18 cm in  
298 diameter) and are embedded in a matrix of medium-to-coarse ash. This pumice-rich massive  
299 ignimbrite facies is poorly sorted and contains small amounts of lithic fragments of dacitic ignimbrite  
300 (Fig. 7f) up to 65 cm in length and dense grey juvenile fragments. They have diffuse margins that  
301 grade continuously into the enclosing massive ignimbrite. This ignimbrite is about 4 m thick but its  
302 lateral extension – probably of just a few metres – is imprecise as it only appears as eroded  
303 discontinuous outcrops.

304

## 305 **5. Depositional model**

### 306 *5.1 Model design*

307 The importance of accumulation rates and velocities is increasingly being recognised not only  
308 for volcanic deposits but also for sedimentary deposits in general (e.g., Lowe, 1988; Kneller and  
309 Branney, 1995; Girolami et al., 2010; Doronzo et al., 2012, 2017; Breard et al., 2016; Dellino et al.,  
310 2019). The theoretical model we develop here aims to estimate the accumulation rates of the Coranzulí  
311 ignimbrite deposits by inverting the field deposit thicknesses and introducing a dimensionless  
312 temperature that expresses the variation rate of temperature during emplacement. This should be  
313 regarded as a reverse engineering problem, in which the dense PDC is not directly modelled.  
314 Conceptually, we approximate the depositional system of the dense PDC as a dense single-phase flow,  
315 which supplies sediment for the growing deposit (see Legros and Martí, 2001; Roche, 2015).

316 The first equation of the model defines the accumulation rate  $A_r$  from the dense PDC as the  
317 rate at which the final deposit builds up from the substrate to the surface (after Doronzo et al., 2016;  
318 Giordano and Doronzo, 2017; see also Martí et al., 2019, for application to welded deposits)

$$319 \quad A_r = \frac{T_{dep}}{T_p} \frac{h\rho_p}{t} \quad (\text{Eq. 1})$$

320

321 where the deposit thickness  $h$  refers to the cumulative or total deposit emplaced by various  
322 flow pulses (each one emplacing a depositional unit, i.e., lamina, massive layer),  $\rho_p$  is the average  
323 density of all the particles involved,  $t$  is the emplacement timescale,  $T_{dep}$  is the average temperature of  
324 the flow at emplacement, and  $T_p$  is the particle (weighted average of juvenile and lithic fragments)  
325 temperature. Thus, Eq. 1 contains an accumulation velocity,  $h/t$ , and a dimensionless temperature,  
326  $T_{dep}/T_p$ . Following Sulpizio and Dellino (2008) and Doronzo and Dellino (2014), we separate the  
327 concept of ‘flow’ from that of ‘current’, which implies that various flow pulses, i.e., individual  
328 pyroclastic flows, could have sustained the currents that generated the Coranzulí ignimbrites (a time-  
329 dependent issue). We consider the deposit thickness as local as we cannot rule out the possibility that  
330 more than one current (probably from different ring-fault sectors; see Seggiaro et al., 2019) formed the  
331 final deposit by overlapping at a specific site (a space-dependent issue). Another limitation is that the  
332 deposit thickness likely represents a minimum thickness, because some erosion could have occurred in  
333 an arid region like Altiplano-Puna. This is a common issue in stratigraphy in general, particularly

334 when relatively old rocks are involved, and when erosion rates are difficult to assess. On the other  
335 hand, we consider the whole studied pyroclastic sequence as built up in a single eruption, which  
336 implies that the proportion between the different ignimbrite units could have not been particularly  
337 affected by erosion. For the dimensionless temperature, we consider two opposite cases: (i)  $T_{dep} < T_p$ ,  
338 whereby the pyroclasts cool down in relation to their initial temperature (heat loss) without ever  
339 falling below the glass transition temperature (Martí et al., 1991); and (ii)  $T_{dep} > T_p$ , whereby the  
340 pyroclasts heat up in relation to their initial temperature (strain heating) and stay reasonably above the  
341 glass transition temperature (Robert et al., 2013). In order to take into account both thermal cases, we  
342 consider a range of  $T_{dep}/T_p$  of 0.7–1.5, which is compatible with reduced flow dilution within the dense  
343 PDC (Walker, 1972; see also Girolami et al., 2015).

344         The timescale of the emplacement of the ignimbrites (from substrate to surface) depends not  
345 only on the duration of the eruption but also on local depositional mechanisms affected by topography  
346 (Branney and Kokelaar, 2002; Sulpizio et al., 2014). In large volume eruptions, the substrate involved  
347 during the deposition, i.e., the paleotopography, is most of the times completely covered by the  
348 resulting deposits. This happens in our case study, so the best way to account for flow-topography  
349 interaction is to focus on the relative proportions of local deposit thicknesses (see next equation) and  
350 facies variations as a function of the accumulation rate. In these eruptions, however, paleotopography  
351 can locally affect the deposition only when inertia dominates in flow transportation (Doronzo, 2012;  
352 Roche, 2012; see discussion). At a specific site, the emplacement timescale must be shorter than the  
353 entire duration of the eruption,  $t_{erupt}$ , as there is no deposition between the onset of the eruption and the  
354 passage of the dense PDC away from the site (Rowley et al., 2014; Platzman et al., 2020). This is also  
355 valid for very proximal zones where the pyroclastic sediment is somehow laterally displaced under the  
356 action of Mass Eruption Rate (Roche, 2012; Roche et al., 2016; Giordano and Doronzo, 2017;  
357 Sweeney and Valentine, 2017; Dellino et al., 2019). In particular, we refer to  $t_{erupt}$  as the duration of  
358 pyroclastic flow phase, from generation to emplacement in a single eruption, which in our case study  
359 coincides with the entire eruption duration as for the absence of an early Plinian phase. The broad  
360 inequality  $t < t_{erupt}$  will account for the complex mechanisms of deposit formation given that the onset  
361 of the emplacement from the depositional system, i.e., the decoupling of the sediment from the flow,

362 should be regarded as very rapid (Roche, 2012; see also Sulpizio et al., 2007; Sulpizio and Dellino,  
363 2008; Doronzo, 2012; Breard et al., 2016; Platzman et al., 2020). For the Coranzulí eruption, we  
364 assume a range of  $t_{erupt}$  of 5–50 h, which is reasonable for a large sustained explosive eruption (Self,  
365 2006; Costa and Martí, 2016).

366 The second equation calculates approximately the emplacement timescale as the product of  
367 the entire eruption and a dimensionless thickness,  $h_{sz}/h$

368

369  $t \approx \frac{h_{sz}}{h} t_{erupt}$  (Eq. 2)

370

371 A word of caution must be spent with reference to the direct application of Eq. 2.  
372 Macroscopically, we assess that the dimensionless thickness can be appropriate for scaling the  
373 eruption duration to the emplacement timescale because  $h$  is the total deposit thickness, while the  
374 shear zone thickness,  $h_{sz}$ , defines the level of upward migration, from substrate to top, of the  
375 depositional system subject to strain rate within the pyroclastic flows. The shear zone thickness can  
376 also be regarded as the thickness of the depositional unit, which for the Coranzulí ignimbrites is of the  
377 order of meters to tens-of-meters related to the massive units of the pyroclastic flow deposits (layer up  
378 to 1 m, bed > 1 m). The concept around Eq. 2 is that no deposition occurs in a site until the pyroclastic  
379 flow reaches that site, and this justifies the inequality between  $t$  and  $t_{erupt}$ . Then, each flow emplaces its  
380 own depositional unit, and the sum of the depositional units defines the total deposit at that site, and  
381 this justifies the inequality between  $h_{sz}$  and  $h$ . Considering that the temporal scale in sedimentary  
382 systems is recorded in vertical direction in the deposits, we are confident that  $h_{sz}/h$  is appropriate for  
383 capturing the deposit growth and level of upward migration at the site (through  $t$ ) as the eruption  
384 progresses and feeds the dense currents at the vent (through  $t_{erupt}$ ). Generally,  $h_{sz} \ll h$  (Doronzo and  
385 Dellino, 2013; Robert et al., 2013; Martí et al., 2017; Dellino et al., 2019), from which we can derive  
386 the inequality  $t \ll t_{erupt}$ , which means that the final deposit at a specific site can form in a time that is  
387 shorter than the entire eruption duration (see also Lavallée et al., 2015; Platzman et al., 2020). This is  
388 reasonable during large ignimbrite- and caldera-forming eruptions, since a substantial amount of the

389 sediment is deposited ahead of the site, as it spreads out from the caldera rim under the action of Mass  
390 Eruption Rate (Costa and Martí, 2016; Giordano and Doronzo, 2017).

391 The third equation of the model gives the accumulation rate by combining Eq. 2 and Eq. 1

392 
$$A_r = \frac{T_{dep} h^2 \rho_p}{T_p h_{sz} t_{erupt}} \quad (\text{Eq. 3})$$

393

394 This equation enables us to conduct a parametric study of a theoretical reference scenario for  
395 the Coranzulí eruption, using the following ranges:  $0.7 \leq T_{dep}/T_p \leq 1.5$ ,  $5 \leq t_{erupt} \leq 50$  h, and  $1 \leq h_{sz} \leq 2$   
396 m. Equation 3 does not consider the eruption rate as it does not directly influence the accumulation  
397 rate for large volume eruptions. In particular, the entire eruption duration will account for the  
398 cumulative dispersion of dense PDCs during the pulsating caldera collapse event, while the shear zone  
399 thickness will account for flow-deposit interface in which the strain rate is the highest (cf., Roche,  
400 2012; Rowley et al., 2014). We chose such ranges to keep the model as general as possible, then the  
401 described stratigraphy will constrain the application to our case study.

402

## 403 5.2 Model description

404 We first examine a reference scenario for a theoretical large explosive eruption and then  
405 compare it with the Coranzulí case study. In particular, we use as an example an eruption of several  
406 hundreds of km<sup>3</sup> of silicic magma, with Mass Eruption Rates of 10<sup>9</sup>–10<sup>11</sup> kg/s, lasting from a few  
407 hours to a few days (Costa and Martí, 2016). Within this timeframe, there is time for the emplacement  
408 of ignimbrites under the inequality  $t \ll t_{erupt}$  (Lavallée et al., 2015; Platzman et al., 2020). We also  
409 assume a single deposit thickness of 100 m and a particle density of 2000 kg/m<sup>3</sup>. In Fig. 8, the  
410 accumulation rate is plotted as a function of the dimensionless temperature in a range  $h_{sz} \cdot t_{erupt}$  of 5–100  
411 m·h. These two values correspond to the extreme cases  $h_{sz}(\text{min}) \cdot t_{erupt}(\text{min})$  and  $h_{sz}(\text{max}) \cdot t_{erupt}(\text{max})$ ,  
412 respectively, while all possible combinations lie in between these extremes (shaded area in Fig. 8).

413 The physical meaning of Fig. 8 is that the shorter the eruption, the faster the formation of the  
414 deposit. The slowest scenario gives an accumulation velocity of 28 mm/s and a minimum  
415 accumulation rate of 39.2 kg/m<sup>2</sup> s, while the fastest gives an accumulation velocity of 550 mm/s and a

416 minimum accumulation rate of  $770 \text{ kg/m}^2 \text{ s}$ . These values give broad ranges for these two quantities  
417 due to the variability in the duration of the eruption and indicate that (i) accumulation velocities of  $\geq 28$   
418 mm/s are typical of dense PDCs emplacing ignimbrites by rapid progressive aggradation; and (ii)  
419 accumulation velocities of  $550 \text{ mm/s}$  are typical of dense PDCs emplacing ignimbrites by rapid *en*  
420 *masse* emplacement. Such orders of magnitude have been reported in large-scale laboratory  
421 experiments with dense PDCs (e.g., Roche, 2012; Rowley et al., 2014; Girolami et al., 2015; Breard et  
422 al., 2016; Breard and Lube, 2017; Sulpizio et al., 2016). Thus, the dominant mode of emplacement of  
423 ignimbrites will be either rapid progressive aggradation or rapid *en masse* emplacement, depending on  
424 the eruption timescale. Nonetheless, a combination of these two modes will probably occur in any  
425 single large eruption, as the accumulation rate changes over space (due to local topography) and time  
426 (due to the pulsating event).

427 Finally, the intercept  $T_{dep}/T_p = 1$  in Fig. 8 separates the fields characterised by heat loss ( $T_{dep}/T_p$   
428  $< 1$ ) and strain heating ( $T_{dep}/T_p > 1$ ). The physical meaning of the relationship between the accumulation  
429 rate and the dimensionless temperature is that the faster the accumulation, the more thermally  
430 conservative the deposit (cf., Michol et al., 2008; Lavallée et al., 2015; Doronzo et al., 2016; Giordano  
431 and Doronzo, 2017; Trolese et al., 2017; Martí et al., 2019). For example, welded ignimbrites will  
432 form at relatively high accumulation rates, whereas lava-like lithofacies will occur at extremely high  
433 accumulation rates ( $\sim 1000 \text{ kg/m}^2 \text{ s}$ ). We suspect that the latter case is most likely to occur in intra-  
434 caldera settings under highly sustained pyroclastic fountaining.

435

## 436 **6. Discussion**

437

### 438 *6.1. Deposits and flow characteristics*

439 The Coranzulí Caldera formed about 6.6 Ma ago and generated  $650 \text{ km}^3$  of crystal-rich dacite  
440 ignimbrite deposits, which are distributed to the north, northwest, east and south (Fig. 2) over an area  
441 of  $2050 \text{ km}^2$  (Seggiaro et al., 1987, 2019). This caldera-forming eruption has recently been interpreted  
442 as a pulsating boiling-over event in which the caldera collapse developed immediately after the onset  
443 of the eruption, favoured by a transtensive tectonic system (Seggiaro et al., 2019). Under these

444 conditions, caldera collapse was not homogeneous, occurring along different sectors of the ring fault  
445 as subsidence progressed, as indicated by the presence of the massive lithic breccia facies, which can  
446 be interpreted as co-ignimbrite lag breccias (Seggiaro et al., 1987) with different lithic components at  
447 the base of each ignimbrite unit.

448 In figure 9 we present an integrated interpretation of the facies architecture of Coranzulí  
449 ignimbrites based on the sum of new and published (Seggiaro et al., 2019, and references therein)  
450 stratigraphic logs. This schematic representation highlights the vertical and lateral facies variations of  
451 Coranzulí ignimbrites discussed below. The distribution of the ignimbrite units in different directions  
452 from the caldera rim are related with the interpreted caldera collapse dynamics by Seggiaro et al  
453 (2019).

454 The absence of Plinian fallout deposits, as has been observed in many other calderas in the  
455 Central Andes (e.g., Cerro Galán: Sparks et al., 1985, Cas et al., 2011; Vilama: Soler et al., 2007;  
456 Aguas Calientes: Petrinovic et al., 2010; Luingo: Guzmán and Petrinovic, 2010), and the relatively  
457 low depletion of fines through elutriation indicate that the flows that fed the pyroclastic currents were  
458 mostly concentrated and not much thicker than their resulting deposits (Seggiaro et al., 2019). The  
459 presence of the fine-grained cross-stratified facies in some proximal settings (Fig. 9) can be interpreted  
460 as the result of locally diluted flows, dominated by traction during their emplacement (e.g., ignimbrite  
461 unit 1), which could be the result of their deposition on a steep slope after flow-topography interaction  
462 (e.g., Branney and Kokelaar, 2002; Sulpizio et al., 2014; Giordano and Doronzo, 2017). It is even  
463 possible to find these same lithofacies at significant distances from source, depending on the  
464 morphology of the substrate, and wherever the flows were not directly affected by the Mass Eruption  
465 Rate but, instead, influenced mainly by their own inertia (Roche, 2015; Giordano and Doronzo, 2017).  
466 These are the main physical conditions to have flow-topography interaction as effective in large  
467 volume pyroclastic flows and associated deposits. It is to remark once again that in our case study the  
468 whole pyroclastic sequence covers the paleotopography in most outcrops. In the fine-grained cross-  
469 stratified facies of ignimbrite unit 1 to the north of the caldera some lenticular lithic-rich facies were  
470 identified in the stratified succession. As these deposits are very proximal, we believe that they were  
471 derived from drag forces that picked up lithics from the substrate, which were then locally deposited

472 by granular jumps (cf., Martí et al., 2019). This hypothesis is supported by the character and  
473 composition of the fragments (rounded to subrounded fragments of dacites and metapelites and  
474 quartzites from the Ordovician basement). However, we cannot exclude that some lithics could also  
475 derive from erosion of the caldera wall due to the caldera collapse and successive caldera enlargement.  
476 These deposits, which are very localised, may correspond to an initial explosive phase that locally  
477 preceded the opening of the ring fault. This is suggested by the fact that in ignimbrite unit 1 this  
478 deposit grades transitionally into the massive lithic breccia facies rich in dacitic lava lithics, which can  
479 be interpreted as a co-ignimbritic lithic lag breccia that gradually changes into the massive ignimbrite  
480 facies. The massive ignimbrite can be interpreted as having formed under flow boundary zones that  
481 are transitional between granular and fluid-escape-dominated flows.

482         The massive lithic breccia facies at their base in proximal zones was interpreted by Seggiaro et  
483 al (2019) as a co-ignimbritic lag breccia representing the opening (or widening) of conduits within the  
484 area of the caldera rim. In some logs (see log 1 and 15 in Fig. 3a,d, 9c) the base of these ignimbrite  
485 units has a fine-grained cross-stratified facies that is the result of traction-dominated parental flows,  
486 probably after flow-topography interaction (inertia condition; Doronzo, 2012; Roche, 2012). As with  
487 Ignimbrite unit 1, the massive ignimbrite facies in units 2, 3 and 4 were formed under flow boundary  
488 zones that were transitional between granular and fluid-escape-dominated flows.

489         In Ignimbrite unit 2, of note is the lenticular lithic-rich facies up to 2 m thick found at about 18  
490 km to the northwest of the caldera rim (Fig. 9c), which has transitional contacts with the massive  
491 ignimbrite facies in which it is enclosed; blocks are up to 30 cm in diameter. Similar lithic-rich lenses  
492 have been described from other ignimbrites (e.g., Le Pennec et al., 1994). Recently, Roche (2015)  
493 performed experimental analyses in an attempt to understand the conditions required for the formation  
494 of this facies tens of kilometres from its source. This author's experiments show that clast sizes  
495 entrained by dilute currents reach up to 15 cm in diameter but that entrainment by a PDC consisting of  
496 a dense basal flow with high interstitial gas pore pressure can uplift even bigger substrate particles –  
497 due to the upward pressure gradient at the flow-substrate interface – and then transport and deposit  
498 them in the basal deposit of the flow by granular jumps (cf., Martí et al., 2019). Roche (2015) derived  
499 a velocity of the parent dense PDCs of up to ~25–30 m/s for ignimbrites with lithics up to 2 m. We

500 applied Roche's (2015) equation 8 using the features of the largest fragment in a lenticular lithic-rich  
501 facies at a flow front. We considered a density of  $2700 \text{ kg/m}^3$  for a quartzite lithic fragment of  
502 ellipsoidal shape with a minor axis of 0.25 cm, and assumed a current bulk density of  $1400 \text{ kg/m}^3$  and  
503 a density of the interstitial fluid of  $1 \text{ kg/m}^3$ . We obtained a velocity of 7.43 m/s for the PDCs of  
504 Coranzulí, which is similar to those of the Galán ignimbrites (~8–10 m/s) (Roche, 2015, and  
505 references therein). This is further evidence of the mobility of the flows that formed the Coranzulí  
506 ignimbrites and implies that they were highly concentrated PDCs that were moving at relatively low  
507 velocities.

508 In similar way, it is worth mentioning the presence in some ignimbrite units of a pumice-rich  
509 massive ignimbrite facies (see log 17 in Fig. 3d). This is thought to have formed at a flow boundary  
510 zone dominated by granular flow, a theory backed by the massive character of the ignimbrite, the  
511 absence of elutriation pipes, and the relatively similar crystal contents within the pumices and matrix.  
512 Hence, the pumice may have segregated as flotsam because of their inability to percolate down into  
513 the granular flow (e.g., Branney and Kokelaar, 2002). They may have travelled long distances as a  
514 result of this overpassing (see distal facies of ignimbrite unit 4 in Fig. 3d, 9d). However, the presence  
515 of some lithics up to 65 cm in length in this sequence (see Fig. 7f) and the poor sorting of the pumice  
516 (Fig. 7g) may indicate that these pumice were deposited as flotsam and were immediately remobilised  
517 by a subsequent, more concentrated part of the flow capable of transporting large blocks. These  
518 blocks, once deposited, settled down in the recently sedimented pumice-rich layer. The above-  
519 mentioned blocks of ignimbrites are indistinguishable in composition from those of the Coranzulí  
520 ignimbrites, which thus may indicate that these fragments were part of an ignimbrite that is  
521 compositionally similar to and slightly older than those from Coranzulí. Evidence for the occurrence  
522 of older ignimbrites of similar compositions to those from Coranzulí can be found nearby, as for  
523 example in the Morro Grande ignimbrites (López et al., 2016).

524

## 525 *6.2. Model application*

526 To apply this model to the Coranzulí ignimbrites we used our field measurements of the local  
527 deposit thicknesses – we chose not to consider a single thickness as representative of the whole

528 deposit (reference scenario) – to calculate site-by-site the corresponding accumulation rates. From  
529 each measurement, we also calculated the accumulation velocities and the emplacement timescales  
530 (Table 1). The results shown in Fig. 8 refer to a theoretical large explosive eruption with uniform  
531 emplacement (single deposit thickness). In Table 1, however, we highlight the spatial variability in the  
532 emplacement of the Coranzulí deposits (local thicknesses). It is to mention, as explained in the  
533 formulation of the model, that the local deposit thicknesses are to be considered as minimum  
534 thicknesses, as we cannot exclude that erosion occurred over the 6.6 Ma, which is a general issue for  
535 volcanic successions in explosive volcanism.

536         When considering the general characteristics of the Coranzulí ignimbrites, we took into  
537 account two important factors: (i) each local measurement corresponds to the total thickness of the  
538 deposit on a site-by-site basis as it was impossible to know precisely whether or not all dense currents  
539 (each one giving rise to an ignimbrite unit) reached all the sites during the pulsating caldera collapse  
540 event; and (ii) given that the Coranzulí deposits are mostly moderately welded, we first excluded  
541 strain heating (Fig. 8) and then opted for  $T_{dep}/T_p = 0.7$ , which is still a thermally conservative case. The  
542 first factor gives qualitative results, with the limitation that the accumulation rates change over time.  
543 The second factor relates to the textural characteristics of the deposits, which are far from being  
544 strongly welded, high-grade or lava-like ignimbrites (cf., Wilson and Hildreth, 2003; Quane and  
545 Russell, 2005; Michol et al., 2008; Robert et al., 2013; Pacheco-Hoyos et al., 2018).

546         Table 1 reveals that the thicker the deposit, the faster its accumulation. The slower cases give  
547 accumulation velocities of  $<10$  mm/s and accumulation rates of  $<12$  kg/m<sup>2</sup> s. These cases are the  
548 minority and, except for log 10, correspond to the most distal sites of the Coranzulí deposits. By  
549 contrast, the faster cases have accumulation velocities of  $>20$  mm/s and accumulation rates of  $>28$   
550 kg/m<sup>2</sup> s. These cases are the majority and correspond to the proximal and medial-to-distal sites of the  
551 ignimbrite deposits. Each case defines a broad range of the two calculated quantities due to the  
552 variability of the duration of the entire eruption. These ranges vary due to variability in the thicknesses  
553 of the local deposits, which shows that, while at some sites the formation of the Coranzulí ignimbrites  
554 was slow, at others it was swift (maximum accumulation velocities  $>350$  mm/s). In particular,

555 minimum accumulation velocities of >50 mm/s for logs 5 and 9 indicate that the local accumulation  
556 was rapid.

557         The Coranzulí ignimbrite sequence is very thick and conceals the paleotopography and so the  
558 application of the depositional model only allows us to infer general flow dynamics: (i) dense currents  
559 led to the Coranzulí ignimbrites piling up over time during a sustained large explosive eruption, i.e.,  
560 for the duration of the whole eruption (caldera scale); and (ii) each pyroclastic flow sustaining a  
561 current emplaced the various depositional units by rapid accumulation, and the facies variations in the  
562 deposits were likely also dependent on local paleotopography (cf., Sparks et al., 1973; Doronzo, 2012;  
563 Roche, 2012; Sulpizio and Dellino, 2008; Martí et al., 2017, 2019).

564         Our theoretical model of long-lived, large-volume dense PDCs emplacing the Coranzulí  
565 ignimbrites gives a threshold for the accumulation rate of  $\geq 39.2 \text{ kg/m}^2 \text{ s}$ . Such an order of magnitude  
566 is found in large-scale laboratory experiments carried out on dense PDCs (Roche, 2012; Girolami et  
567 al., 2015; Breard et al., 2016). On the other hand, a threshold for the accumulation rate of  $< 5 \text{ kg/m}^2 \text{ s}$   
568 has been derived from recent 3D numerical simulations and experiments on short-lived, small-volume  
569 PDCs (Doronzo et al., 2017; Dellino et al., 2019). These two accumulation rates, which diverge in  
570 orders of magnitude, are thought to be responsible for the emplacement of massive versus laminated  
571 deposits at local scales, respectively (Doronzo et al., 2017; Giordano and Doronzo, 2017; Dellino et  
572 al., 2019). Conversely, the eruptive conditions for the formation of a PDC are important at a volcano  
573 scale (Doronzo et al., 2016; Sweeney and Valentine, 2017). In particular, low values for the  
574 accumulation rates will correspond to small- to intermediate-volume dilute PDCs, which lose a  
575 substantial amount of solid load in proximal areas due to short-lived, vertical column collapse and  
576 ground impact (Doronzo et al., 2017; Dellino et al., 2019; Navarrete et al., 2020).

577         The resulting goal after applying the theoretical model is to relate the emplacement  
578 mechanisms to the eruptive mechanisms at Coranzulí. In this sense, our model is consistent with a  
579 sustained large-volume explosive eruption, in which dense PDCs formed as a consequence of low,  
580 dense pyroclastic fountaining with retained temperature and reduced air entrainment (Sparks and  
581 Wilson, 1976; Bursik and Woods, 1996; Guzmán and Petrinovic, 2010; Petrinovic et al., 2010; Dufek,  
582 2016; Pacheco-Hoyos et al., 2018; Dellino et al., 2019). Other similar caldera-forming events show

583 that the application of the model to the Coranzulí case study is consistent with cases such as Cerro  
584 Galán (Cas et al., 2011), Vilama (Soler et al., 2007), Aguas Calientes (Petrinovic et al., 2010) and La  
585 Pacana (Lindsay et al., 2001a), which all have similar field characteristics. The absence of Plinian  
586 fallout deposits preceding the emplacement of the four ignimbrite units – and the very low elutriation  
587 of fine-grained particles – support this view (Walker, 1972) and argue against the existence of a high-  
588 rising then collapsing vertical column with associated dilute PDCs, as occurs more frequently in  
589 small-volume eruptions (cf., Sulpizio et al., 2014; Roche, 2015; Navarrete et al., 2020). The general  
590 conceptual model that derives from the Coranzulí case study is thus that of dense PDCs emplacing  
591 large ignimbrites during a sustained large-volume eruption (Cas et al., 2011; Ort et al., 2013; Willcock  
592 et al., 2013; Sulpizio et al., 2014; Costa and Martí, 2016; Roche et al., 2016; Trolese et al., 2017;  
593 Pacheco-Hoyos et al., 2018) dominated by forced convection (Doronzo, 2012; Giordano and Doronzo,  
594 2017), in which local topography enhances flow inertia and deposit facies variation in  
595 correspondence of the fine-grained cross-stratified facies (Doronzo, 2012; Roche, 2012).

596

## 597 **Conclusions**

598

599 The Coranzulí Caldera (23°00'S-66° 15'W) generated four thick, crystal-rich (30–60%)  
600 ignimbrite units with varying pumice (usually >20%) and lithic clast (from <7% to >25%) content.

601 The caldera eruption occurred in different pulses in different sectors of the ring fault and  
602 generated very low dense eruption columns with little air entrainment that collapsed almost  
603 immediately and continuously. This was then succeeded by concentrated PDCs that travelled at  
604 relatively low velocities (less than tens of m/s). These PDCs were dominated by granular-to- (less  
605 frequently) fluid-escape-dominated flow boundary zones that generated the massive ignimbrite facies.  
606 Some minor pauses in the eruption are revealed by the presence of sudden contacts between lithofacies  
607 and by the presence of small co-ignimbritic ash-cloud surges such as those identified by Seggiaro et al.  
608 (2019). Throughout each of the ignimbrite units, different lithofacies including co-ignimbritic lag

609 breccias, fine-grained stratified facies, and prominent massive lithofacies are visible, thereby  
610 indicating the presence of different mechanisms of transport and deposition for these currents.

611 Our theoretical model allows us to explain these very different types of flow behaviour. The  
612 fine-grained proximal lithofacies was formed by locally diluted flows, with flow boundary zones  
613 dominated by traction during their deposition on a steep slope. These stratified lithofacies are the  
614 minority and correspond to flow emplacements under relatively low accumulation rates, as derived  
615 from the theoretical model applied to the Coranzulí case study. By contrast, the massive lithofacies  
616 corresponds to flow emplacement with high accumulation rates, when pyroclastic flows were still far  
617 travelling under the effects of Mass Eruption Rate during the sustained eruption. In particular, some  
618 alternation of stratified and massive thin sets of deposits in proximal settings probably reflects  
619 oscillatory flow-boundary conditions, varying from a fluid-escape-/granular-flow-dominated flow  
620 boundary zone to a traction-flow-dominated boundary zone. These conditions can be related to the  
621 unsteadiness associated with dynamical changes in topography, which in turn are probably related to  
622 the mechanisms of the syn-eruptive subsidence and the widening of the caldera rim. In other words,  
623 the topography was changing during the eruption itself. On the other hand, lithic-rich lenses were  
624 formed by the uplift of substrate blocks by a dense basal flow with high interstitial gas pore pressure,  
625 which was able to transport and deposit these blocks on the basal deposit of the flow.

626 The depositional model derived from the study of the Coranzulí ignimbritic succession, which  
627 is particularly thick and conceals the paleotopography, can also be applied to infer general flow  
628 dynamics from other similar large-volume, crystal-rich, caldera-forming ignimbrites in the same area.  
629 These large ignimbrites were, in the majority, emplaced by pyroclastic flows by rapid accumulation in  
630 a long-lived eruption dominated by forced convection, while their internal facies variations were, in  
631 the minority, influenced by local paleotopography.

632

### 633 **Acknowledgements**

634 This work was supported by Agencia Nacional de Promoción Científica y Técnica (PICT-2012-419;  
635 PICT-2017-2798; PICT-2017-1928) and the Consejo Nacional de Investigaciones Científicas y  
636 Técnicas (PUE 2016-2021), Argentina. SG is grateful to Elena López, Albano Floridia and Emanuel

637 Ramos for their assistance in the field and Valmir da Silva Souza for the helpful discussions. JM is  
638 supported by the Spanish Grant CGL2017-84901-C2-1. We thank the constructive reviews of two  
639 anonymous referees, and the editor, Jasper Knight. English text was reviewed and corrected by  
640 Michael Lockwood.

641

## 642 **References**

643

644 Allmendinger, R., Gubbels, T., 1996. Pure and simple shear plateau uplift, Altiplano– Puna, Argentina  
645 and Bolivia. *Tectonophysics* 259, 1–13.

646 Alonso, R., 1986. Ocurrencia, posición estratigráfica y génesis de los depósitos de boratos de la Puna  
647 Argentina (Ph.D. thesis). Universidad Nacional de Salta, Argentina.

648 Branney, M.J., Kokelaar, B.P., 2002. Pyroclastic density currents and the sedimentation of  
649 ignimbrites: *Geological Society of London Memoirs* 27, London.

650 Breard, E.C.P., Lube, G., 2017. Inside pyroclastic density currents—Uncovering the enigmatic flow  
651 structure and transport behaviour in large-scale experiments. *Earth and Planetary Science Letters*  
652 458, 22–36.

653 Breard, E.C.P., Lube, G., Jones, J.R., Dufek, J., Cronin, S.J., Valentine, G.A., Moebis, A., 2016.  
654 Coupling of turbulent and non-turbulent flow regimes within pyroclastic density currents. *Nature*  
655 *Geoscience* 9, 767–771.

656 Bursik, M.I., Woods, A.W., 1996. The dynamics and thermodynamics of large ash flows. *Bulletin of*  
657 *Volcanology* 58, 175–193.

658 Cas, R.A.F., Wright, J.V., 1987. *Volcanic Successions Modern and Ancient: a geological approach to*  
659 *processes, products and successions*. Allen & Unwin, London.

660 Cas, R.A.F., Wright, H.M.N., Folkes, C.B., Lesti, C., Porreca, M., Giordano, G., Viramonte, J.G.,  
661 2011. The flow dynamics of an extremely large volume pyroclastic flow, the 2.08-Ma Cerro Galán  
662 Ignimbrite, NW Argentina, and comparison with other flow types: *Bulletin of Volcanology* 73,  
663 1583–1609.

664 Caffè, P.J., Soler, M.M., Coira, B.L., Onoe, A.T., Cordani, U.G., 2008. The Granada ignimbrite: a  
665 compound pyroclastic unit and its relationship with Upper Miocene caldera volcanism in the  
666 northern Puna. *Journal of South American Earth Sciences* 25, 464–484.

667 Chmielowski, J., Zandt, G., Haberland, C., 1999. The central Andean Altiplano-Puna magma body.  
668 *Geophysical Research Letters* 26, 783–786.

669 Coira, B., 1973. Resultados preliminares sobre la petrología del ciclo eruptivo ordovícico  
670 concomitante con la sedimentación de la Formación Acoite en la zona de Abra Pampa, Provincia  
671 de Jujuy, Argentina. *Revista de la Asociación Geológica Argentina* 28, 85–90.

672 Coira, B.L., Kay, S.M., Viramonte, J.G., 1993. Upper Cenozoic magmatic evolution of the Argentine  
673 Puna - a model for changing subduction geometry. *International Geological Reviews* 35, 677-720.

674 Costa, A., Martí, J., 2016. Stress field control during large caldera-forming eruptions. *Frontiers in*  
675 *Earth Science* 4, 92, doi:10.3389/feart.2016.00092.

676 de Silva, S.L., 1989. Altiplano–Puna Volcanic Complex of the Central Andes. *Geology* 17, 1102–  
677 1106.

678 de Silva, S.L., Riggs, N.R., Barth, A.P., 2015. Quickening the pulse: Fractal tempos in continental arc  
679 magmatism. *Elements* 11, 113–118.

680 Dellino, P., Dioguardi, F., Doronzo, D.M., Mele, D., 2019. The rate of sedimentation from turbulent  
681 suspension: an experimental model with application to pyroclastic density currents and discussion  
682 on the grain-size dependence of flow runout. *Sedimentology* 66, 129–145.

683 Doronzo, D.M., 2012. Two new end members of pyroclastic density currents: forced convection-  
684 dominated and inertia-dominated. *Journal of Volcanology and Geothermal Research* 219-220, 87–  
685 91.

686 Doronzo, D.M., Dellino, P., 2013. Hydraulics of subaqueous ash flows as deduced from their  
687 deposits: 2. Water entrainment, sedimentation, and deposition, with implications on pyroclastic  
688 density current deposit emplacement. *Journal of Volcanology and Geothermal Research* 258, 176–  
689 186.

690 Doronzo, D.M., Dellino, P., 2014. Pyroclastic density currents and local topography as seen with the  
691 conveyer model. *Journal of Volcanology and Geothermal Research* 278–279, 25–39.

692 Doronzo, D.M., Martí, J., Sulpizio, R., Dellino, P., 2012. Aerodynamics of stratovolcanoes during  
693 multiphase processes. *Journal of Geophysical Research* 117, B01207, doi: 10.1029/2011JB008769.

694 Doronzo, D.M., Martí, J., Dellino, P., Giordano, G., Sulpizio, R., 2016. Dust storms, volcanic ash  
695 hurricanes, and turbidity currents: physical similarities and differences with emphasis on flow  
696 temperature. *Arabian Journal of Geosciences* 9, 290, doi: 10.1007/s12517-016-2351-8.

697 Doronzo, D.M., Dellino, P., Sulpizio, R., Lucchi, F., 2017. Merging field mapping and numerical  
698 simulation to interpret the lithofacies variations from unsteady pyroclastic density currents on  
699 uneven terrain: the case of La Fossa di Vulcano (Aeolian Islands, Italy). *Journal of Volcanology  
700 and Geothermal Research* 330, 36–42.

701 Druitt, T.H., 1998. Pyroclastic density currents. In: Gilbert, J.S., Sparks R.S.J. (Eds.), *The physics of  
702 explosive eruptions*. Geological Society of London Special Publication 145, pp. 145–182.

703 Dufek, J., 2016. The Fluid Mechanics of Pyroclastic Density Currents. *Annual Review of Fluid  
704 Mechanics* 48, 459–485.

705 Giordano, G., Doronzo, D.M., 2017. Sedimentation and mobility of PDCs: a reappraisal of  
706 ignimbrites' aspect ratio. *Scientific Reports* 7, 4444, doi: 10.1038/s41598-017-04880-6.

707 Girolami, L., Roche, O., Druitt, T.H., Corpetti, T., 2010. Particle velocity fields and depositional  
708 processes in laboratory ash flows, with implications for the sedimentation of dense pyroclastic  
709 flows. *Bulletin of Volcanology* 72, 747–759.

710 Girolami, L., Druitt, T.H., Roche, O., 2015. Towards a quantitative understanding of pyroclastic  
711 flows: Effects of expansion on the dynamics of laboratory fluidized granular flows. *Journal of  
712 Volcanology and Geothermal Research* 296, 31–39.

713 Grocke, S.B., de Silva, S.L., Wallace, P.J., Cottrell, E., Schmitt, A.K., 2017. Catastrophic Caldera-  
714 Forming (CCF) Monotonous Silicic Magma Reservoirs: Constraints from Volatiles in Melt  
715 Inclusions from the 3.49 Ma Tara Supereruption, Guacha II Caldera, SW Bolivia. *Journal of  
716 Petrology* 58, 227–260.

717 Guzmán, S., Petrinovic, I., 2010. The Luingo caldera: the south-easternmost collapse caldera in the  
718 Altiplano–Puna plateau, NW Argentina. *Journal of Volcanology and Geothermal Research* 194,  
719 174–188.

720 Guzmán, S., Grosse, P., Montero-López, C., Hongn, F., Pilger, R., Petrinovic, I.A., Seggiaro, R.,  
721 Aramayo, A., 2014. Spatial-temporal distribution of explosive volcanism in the 25–28°S segment  
722 of the Andean Central Volcanic zone. *Tectonophysics* 636, 170–189.

723 Guzmán, S., Grosse, P., Martí, J., Petrinovic, I.A., Seggiaro, R., 2017. Calderas cenozoicas argentinas  
724 de la Zona Volcánica Central de los Andes – procesos eruptivos y dinámica: una revisión. In:  
725 Muruaga, C.M., Grosse, P. (Eds.), *Ciencias de la Tierra y Recursos Naturales del NOA. Relatorio*  
726 *del XX Congreso Geológico Argentino, San Miguel de Tucumán*, pp. 518-547.

727 Harmon, R.S., Barreiro, B.A., Moorbath, S., Hofes, J., Francis, P.W., Thorpe, R.S., Deruelle, B.,  
728 McHugh, J., Viglino, J.L., 1984. Regional O-, Sr-, and Pb-isotope relationships in late Cenozoic  
729 calcalkaline lavas of the Andean Cordillera. *Journal of the Geological Society of London* 141,  
730 803–822.

731 Iriarte, R., 2012. The Cerro Guacha Caldera Complex: An Upper Miocene-Pliocene Polycyclic  
732 Volcano-Tectonic Structure in the Altiplano Puna Volcanic Complex of the Central Andes of  
733 Bolivia. (Master's thesis). Oregon State University, Corvallis, USA.

734 Isacks, B., 1988. Uplift of the Central Andean Plateau and bending of the Bolivian Orocline. *Journal*  
735 *of Geophysical Research* 93, 3211–3231.

736 Kay, S.M., Mpodozis, C., Coira, B., 1999. Neogene Magmatism, tectonism, and Mineral Deposits of  
737 the Central Andes 22° to 33°S latitude. In: Skinner, B.J. (Ed.); *Geology and Ore Deposits of the*  
738 *Central Andes*. Society of Economic Geologists, Special Publication 7, pp. 27–59.

739 Kay, S., Coira, B., Caffè, P., Chen, C.H., 2010. Regional chemical diversity, crustal and mantle  
740 sources and evolution of Central Andean Puna plateau ignimbrites. *Journal of Volcanology and*  
741 *Geothermal Research* 198, 81–110.

742 Kneller, B.C., Branney, M.J., 1995. Sustained high-density turbidity currents and the deposition of  
743 thick massive sands. *Sedimentology* 42, 607–616.

744 Lavallée, Y., Wadsworth, F.B., Vasseur, J., Russell, J.K., Andrews, G.D.M., Hess, K., von Aulock,  
745 F.W., Kendrick, J.E., Tuffen, H., Biggin, A.J., Dingwell, D.B., 2015. Eruption and emplacement  
746 timescales of ignimbrite super-eruptions from thermo-kinetics of glass shards: *Frontiers in Earth*  
747 *Science* 3, doi:10.3389/feart.2015.00002.

748 Legros, F., Martí, J., 2001. Formation of inversely graded basal layers in ignimbrites by progressive  
749 aggradation. *Journal of Volcanology and Geothermal Research* 111, 25–33.

750 Le Pennec, J.-L., Bourdier, J.-L., Froger, J.-L., Temel, A., Camus, G., Gourgaud, A., 1994. Neogene  
751 ignimbrites of the Nevşehir Plateau (Central Turkey): stratigraphy, distribution and source  
752 constraints. *Journal of Volcanology and Geothermal Research* 63, 59–87.

753 Lesti C, Porreca M, Giordano G, Mattei M, Cas RAF, Wright H, Viramonte J., 2011. High temperature  
754 emplacement of the CerroGalán and Toconquis Group ignimbrites (Puna plateau, NW Argentina)  
755 determined by TRM analyses. In: Cas RAF, Cashman K (eds) *The Cerro Galán Ignimbrite and*  
756 *Caldera: characteristics and origins of a very large volume ignimbrite and its magma system.*  
757 *Bulletin of Volcanology* 73, 1535-1565.

758 Lindsay, J.M., de Silva, S., Trumbull, R., Emmermann, R., Wemmer, K., 2001a. La Pacana caldera,  
759 N. Chile: a re-evaluation of the stratigraphy and volcanology of one of the world's largest resurgent  
760 caldera. *Journal of Volcanology and Geothermal Research* 106, 145–173.

761 Lindsay, J.M., Schmitt, A.K., Trumbull, R.B., de Silva, S.L., Siebel, W., Emmermann, R., 2001b.  
762 Magmatic evolution of the La Pacana caldera system, central Andes, Chile: Compositional  
763 variation of two cogenetic large-volume felsic ignimbrites. *Journal of Petrology* 42, 459–486.

764 López, M.E., Guzmán, S., Seggiaro, R., 2016. Estratigrafía de las ignimbritas de la Formación Morro  
765 Grande, Puna Norte. VII Congreso Latinoamericano de Sedimentología y XV Reunión Argentina  
766 de Sedimentología, La Pampa, Argentina, p. 109.

767 Lowe, D.R., 1988. Suspended-load fallout rate as an independent variable in the analysis of current  
768 structures sedimentology 35, 765–776.

769 Marrett, R., Emerman, S.H., 1992. The relations between faulting and mafic magmatism in the  
770 Altiplano-Puna plateau (Central Andes). *Earth and Planetary Science Letters* 112, 53–59.

771 Martí, J., Diez-Gil, J.L., Ortiz, R., 1991. Conduction model for the thermal influence of lithic clasts in  
772 mixtures of hot gases and ejecta. *Journal of Geophysical Research* 96, 21879–21885.

773 Martí, J., Geyer, A., Folch, A., 2009. A genetic classification of collapse calderas based on field  
774 studies, and analogue and theoretical modelling. In: Thordarson, T., Self, S., Larsen, G., Rowland,  
775 S.K., Hoskuldsson, A. (Eds.), *Studies in Volcanology: The Legacy of George Walker*. Special  
776 Publications of IAVCEI, 2. Geological Society, London, pp. 249–266.

777 Martí, J., Planagumá, L.I., Geyer, A., Aguirre-Díaz, G., Pedrazzi, D., Bolós, X., 2017. Basaltic  
778 ignimbrites in monogenetic volcanism: the example of La Garrotxa volcanic field. *Bulletin of*  
779 *Volcanology* 79, 33, doi:10.1007/s00445-017-1113-0.

780 Martí, J., Doronzo, D. M., Pedrazzi, D., Colombo, F., 2019. Topographical controls on small-volume  
781 pyroclastic flows. *Sedimentology* 66, 2297–2317.

782 McClelland, E., Wilson, C.J.N., Bardot, L., 2004. Paleotemperature determinations for the 1.8 ka  
783 Taupo ignimbrite, New Zealand, and implications for the emplacement history of a high  
784 velocity pyroclastic flow. *Bulletin of Volcanology* 66, 492-513.

785 Michol, K.A., Russell, J.K., Andrews, G.D.M., 2008. Welded block and ash flow deposits from  
786 Mount Meager, British Columbia, Canada. *Journal of Volcanology and Geothermal Research* 169,  
787 121-144.

788 Mon, R., 1979. Esquema tectónico de los Andes del Norte Argentino. *Revista de la Asociación*  
789 *Geológica Argentina* 34, 70–76.

790 Navarrete, C., Butler, K.L., Hurley, M., Marquez, M., 2020. An early Jurassic graben caldera of Chon  
791 Aike silicic LIP at the southernmost massif of the world: The Deseado caldera, Patagonia,  
792 Argentina. *Journal of South American Earth Sciences* 101, 102626, doi:  
793 10.1016/j.jsames.2020.102626.

794 Neri, A., Bevilacqua, A., Esposti Ongaro, T., Isaia, R., Aspinall, W.P., Bisson, M., Flandoli, F.,  
795 Baxter, P. J., Bertagnini, A., Iannuzzi, E., Orsucci, S., Pistolesi, M., Rosi, M., Vitale, S., 2015.  
796 Quantifying volcanic hazard at Campi Flegrei caldera (Italy) with uncertainty assessment: 2.

797 Pyroclastic density current invasion maps. *Journal of Geophysical Research Solid Earth* 120,  
798 2330–2349.

799 Oncken, O., Hindle, D., Kley, J., Elger, K., Victor, P., Schemmann, K., 2006. Deformation of the  
800 Central Andean Upper Plate System-Facts, Fiction, and constraints for plateau models. In: Oncken,  
801 O., Chong, G., Franz, G., Giese, P., Götze, H., Ramos, V., Strecker, M., Wigger, P. (Eds.), *The*  
802 *Andes - Active Subduction Orogeny*. Springer, Berlin, pp. 265–283.

803 Ort, M., 1993. Eruptive processes and caldera formation in a nested downsag collapse caldera: Cerro  
804 Panizos, central Andes Mountains. *Journal of Volcanology and Geothermal Research* 56, 221–252.

805 Ort, M.H., Coira, B.L., Mazzoni, M.M., 1996. Generation of a crust-mantle magma mixture: magma  
806 sources and contamination at Cerro Panizos, central Andes. *Contributions to Mineralogy and*  
807 *Petrology* 123, 308–322.

808 Ort, M.H., de Silva, S.L., Jiménez, N., Jicha, B.R., Singer, B.S., 2013. Correlation of ignimbrites  
809 using characteristic remanent magnetization and anisotropy of magnetic susceptibility, Central  
810 Andes, Bolivia, *Geochemistry Geophysics Geosystems* 14, 141–157.

811 Pacheco-Hoyos, J.G., Aguirre-Díaz, G.J., Dávila-Harris, P., 2018. Boiling-over dense pyroclastic  
812 density currents during the formation of the ~ 100 km<sup>3</sup> Huichapan ignimbrite in Central Mexico:  
813 Stratigraphic and lithofacies analysis. *Journal of Volcanology and Geothermal Research* 349, 268–  
814 282.

815 Pensa, A., Capra, L., Giordano, G., 2019. Ash clouds temperature estimation. Implication on dilute  
816 and concentrated PDCs coupling and topography confinement. *Scientific Reports* 9, 5657,  
817 doi:10.1038/s41598-019-42035-x.

818 Petrinovic, I.A., Martí, J., Aguirre-Díaz, G.J., Guzmán, S.R., Geyer, A., Salado Paz, N., 2010. The  
819 Cerro Aguas Calientes caldera, NW Argentina: an example of a tectonically controlled polygenetic  
820 collapse caldera, and its regional significance. *Journal of Volcanology and Geothermal Research*  
821 194, 15–26.

822 Platzman, E.S., Sparks, R.S.J., Cooper, F.J., 2020. Fabrics, facies, and flow through a large-volume  
823 ignimbrite: Pampa De Oxaya, Chile. *Bulletin of Volcanology* 82, 8, doi:10.1007/s00445-019-  
824 1345-2.

825 Quane, S.L., Russell, J.K., 2005. Ranking welding intensity in pyroclastic deposits. *Bulletin of*  
826 *Volcanology* 67, 129–143.

827 Richards, J.P., Villeneuve, M., 2002. Characteristics of late Cenozoic volcanism along the Archibarca  
828 lineament from Cerro Lulluillaco to Corrida de Cori, Northwest Argentina. *Journal of*  
829 *Volcanology and Geothermal Research* 116, 161–200.

830 Riller, U., Oncken, O., 2003. Growth of the central Andean plateau by tectonic segmentation is  
831 controlled by the gradient in crustal shortening. *Journal of Geology* 111, 367–384.

832 Riller, U., Petrinovic, I., Ramelow, J., Strecker, M., Oncken, O., 2001. Late Cenozoic tectonism,  
833 caldera and plateau formation in the Central Andes. *Earth Planetary Science Letters* 188, 299–311.

834 Robert, G., Andrews, G.D.M., Ye, J., Whittington, A.G., 2013. Rheological controls on the  
835 emplacement of extremely high-grade ignimbrites. *Geology* 41, 1031–1034.

836 Roche, O., 2012. Depositional processes and gas pore pressure in pyroclastic flows: an experimental  
837 perspective. *Bulletin of Volcanology* 74, 1807–1820.

838 Roche, O., 2015. Nature and velocity of pyroclastic density currents inferred from models of  
839 entrainment of substrate lithic clasts. *Earth Planetary Science Letters* 418, 115–125.

840 Roche, O., Phillips, J.C., Kelfoun, K., 2013. Pyroclastic density currents. In: Fagents, S.A., Gregg,  
841 T.K.P., Lopes, R.M.C. (Eds.), *Modeling Volcanic Processes: The Physics and Mathematics of*  
842 *Volcanism*. Cambridge University Press, Cambridge, pp. 203–229.

843 Roche, O., Buesch, D.C., Valentine, G.A., 2016. Slow-moving and far-travelled dense pyroclastic  
844 flows during the Peach Spring super-eruption. *Nature Communications* 7, 10890,  
845 doi:10.1038/ncomms10890.

846 Rowley, P.J., Roche, O., Druitt, T.H., Cas, R.A.F., 2014 Experimental study of dense pyroclastic  
847 density currents using sustained, gas-fluidized granular flows: *Bulletin of Volcanology* 76, 855–  
848 868.

849 Salisbury, M.J., Jicha, B.R., de Silva, S.L., Singer, B.S., Jiménez, N.C., Ort, M.H., 2011.  $^{40}\text{Ar}/^{39}\text{Ar}$   
850 chronostratigraphy of Altiplano-Puna volcanic complex ignimbrites reveals the development of a  
851 major magmatic province. *Geological Society of America Bulletin* 123, 821-840.

852 Salfity, J.A., 1985. Lineamientos transversales al rumbo Andino en el noroeste Argentino. IV  
853 Congreso Geológico Chileno Actas 2, Antofagasta, Chile, pp. 119–137.

854 Seggiaro, R.E., 1994. Petrología, geoquímica y mecanismos de erupción del complejo volcánico  
855 Coranzulí. (Ph. D. thesis). Universidad Nacional de Salta, Argentina.

856 Seggiaro, R., Aniel, B., 1989. Los ciclos piroclásticos cenozoicos del área Tiomayo Coranzulí Jujuy  
857 Argentina. *Revista de la Asociación Geológica Argentina* 44, 394–401.

858 Seggiaro, R., Gorustovich, S., Martí, J., 1987. Las ignimbritas del Complejo Volcánico Coranzulí  
859 (Puna Argentina-Andes Centrales). *Estudios Geológicos* 43, 345–358.

860 Seggiaro, R., Guzmán, S., Martí, J., Montero-López, C., López, E., 2014. Stratigraphy of the Coranzulí  
861 caldera. In: Rocha, R., Pais, J., Kullberg, J. C., Finney, S. (Eds.), *Strati 2013: First International*  
862 *Congress on Stratigraphy. At the cutting edge of stratigraphy*. Springer Geology, Cham, pp. 1269–  
863 1273.

864 Seggiaro, R., Guzmán, S., Martí, J., 2019. Dynamics of caldera collapse during the Coranzulí eruption  
865 (6.6 Ma) (Central Andes, Argentina). *Journal of Volcanology and Geothermal Research* 347,1–12.

866 Self, S., 2006. The effects and consequences of very large explosive volcanic eruptions: Philosophical  
867 *Transactions of the Royal Society A* 364, 2073–2097.

868 Smith, R.L., 1960. Zones and zonal variations in welded ash-flows, US Geological Survey  
869 Professional paper 354-F, Washington, pp. 149-159.

870 Soler, M.M., Caffè, P.J., Coira, B.L., Onoe, A.T., Kay, S.M., 2007. Geology of the Vilama caldera: a  
871 new interpretation of a large-scale explosive event in the Central Andean plateau during the Upper  
872 Miocene. *Journal of Volcanology and Geothermal Research* 164, 23–53.

873 Sparks, R.S.J., Wilson, L., 1976. A model for the formation of ignimbrite by gravitational column  
874 collapse. *Journal of the Geological Society of London* 132, 441–451.

875 Sparks, R.S.J., Self, S., Walker, G.P.L., 1973. Products of ignimbrite eruption. *Geology* 1, 115–118.

876 Sparks, R.S.J., Wilson, L., Hulme, G., 1978. Theoretical modeling of the generation, movement, and  
877 emplacement of pyroclastic flows by column collapse. *Journal of Geophysical Research Solid*  
878 *Earth* 83 (B4), 1727–1739.

879 Sparks, R., Francis, P., Hamer, R., Pankhurst, R., O’Callaghan, L., Thorpe, R. S., Page, R., 1985.  
880 Ignimbrites of the Cerro Galán caldera, NW Argentina. *Journal of Volcanology and Geothermal*  
881 *Research* 24, 205–24.

882 Stern, C.R., 2004. Active Andean volcanism: its geologic and tectonic setting. *Revista Geológica de*  
883 *Chile* 31, 161–206.

884 Sulpizio, R., Dellino, P., 2008. Sedimentology, depositional mechanisms and pulsating behavior of  
885 pyroclastic density currents. In: Martí, J., Gottsman, J. (Eds.), *Caldera volcanism: analysis,*  
886 *modelling and response. Developments in Volcanology*, 10. Elsevier, Amsterdam, pp. 57–96.

887 Sulpizio, R., Mele, D., Dellino, P., La Volpe, L., 2007. Deposits and physical properties of  
888 pyroclastic density currents during complex Subplinian eruptions: the AD 472 (Pollena) eruption  
889 of Somma-Vesuvius, Italy. *Sedimentology* 54, 607–635.

890 Sulpizio, R., Dellino, P., Doronzo, D.M., Sarocchi, D., 2014. Pyroclastic density currents: state of the  
891 art and perspectives. *Journal of Volcanology and Geothermal Research* 283, 36–65.

892 Sulpizio, R., Castioni, D., Rodriguez-Sedano, L.A., Sarocchi, D., Lucchi, F., 2016. The influence of  
893 slope-angle ratio on the dynamics of granular flows: insights from laboratory experiments. *Bulletin*  
894 *of Volcanology* 78, 77, doi:10.1007/s00445-016-1069-5.

895 Sweeney, M. R., Valentine, G. A., 2017. Impact zone dynamics of dilute mono- and polydisperse jets  
896 and their implications for initial conditions of pyroclastic density currents. *Physics of Fluids* 29,  
897 093304, doi:10.1063/1/5004197.

898 Tibaldi, A., Bonali, F., Corazzato, C., 2017. Structural control on volcanoes and magma paths from  
899 local to orogeny-scale: The Central Andes case. *Tectonophysics* 699, 14–41.

900 Trolese, M., Giordano, G., Cifelli, F., Winkler, A., Mattei, M., 2017. Forced transport of thermal  
901 energy in magmatic and phreatomagmatic large volume ignimbrites: paleomagnetic evidence from  
902 the Colli Albani volcano, Italy. *Earth and Planetary Science Letters* 478, 179–191.

903 Trumbull, R.B., Riller, U., Oncken, O., Scheuber, E., Munier, K., Hongn, F., 2006. The time–space  
904 distribution of Cenozoic arc volcanism in the Central Andes: a new data compilation and some  
905 tectonic considerations. In: Oncken, O., Chong, G., Franz, G., Giese, P., Götze, J., Ramos, V.,  
906 Strecker, M., Wigger, P. (Eds.), *The Andes–Active Subduction Orogeny*. *Frontiers in Earth*  
907 *Science Series 1*. Springer-Verlag, Berlin, pp. 29–43.

908 Walker, G.P.L., 1972. Crystal concentration in ignimbrites. *Contributions to Mineralogy and*  
909 *Petrology* 36, 135–146.

910 Willcock, M.A.W., Cas, R.A.F., Giordano, G., Morelli, C., 2013. The eruption, pyroclastic flow  
911 behaviour, and caldera in-filling processes of the extremely large volume ( $> 1290 \text{ km}^3$ ), intra- to  
912 extra-caldera, Permian Ora (Ignimbrite) Formation, Southern Alps, Italy. *Journal of Volcanology*  
913 *and Geothermal Research* 265, 102–126.

914 Wilson, C.J.N., Hildreth, W., 2003. Assembling an ignimbrite: mechanical and thermal building  
915 blocks in the Bishop Tuff, California. *Journal of Geology* 111, 653–670.

916

917 **Figure captions:**

918 Fig. 1. Calderas and caldera-related ignimbrites of the Altiplano-Puna Volcanic Complex, modified  
919 from Petrinovic et al. (2010) and Guzmán et al. (2017).

920

921 Fig. 2. Ignimbrite units from the Coranzulí caldera shown in a Shuttle Radar Topographic Mission  
922 Digital Elevation Model. Black circles with numbers refer to the 20 new stratigraphic logs shown in  
923 Fig. 3 and Table 1.

924

925 Fig. 3. Stratigraphic logs in (a) northern, (b) eastern, (c) northwestern and (d) southern directions from  
926 the caldera.

927

928 Fig. 4. Pre-caldera block and ash flow deposit and ignimbrite unit 1. (a) General view with  
929 monolithologic massive breccia, in which lithics consist only of dacitic lavas, fine-grained cross-  
930 stratified facies, massive lithic breccia facies rich in dacitic lithic fragments with some Ordovician

931 metapelites and quartzites, followed by a massive ignimbrite facies, (b) detail of monolithologic  
932 massive breccia formed by dacitic lithics, (c) detail of fine-grained cross-stratified facies, (d) lithic-  
933 rich lenses within the fine-grained cross-stratified facies, (e) detail of massive lithic breccia facies rich  
934 in dacitic fragments with subordinated Ordovician metapelites and quartzites.

935

936 Fig. 5. (a) Detail of black fiammes, (b) detail of a pink fiamme, (c) detail of crystal-rich pumices in  
937 non-welded facies; a dense juvenile grey fragment is visible in the upper right, (d) detail of grey  
938 fiammes in welded facies.

939

940 Fig. 6. (a, b) Ignimbrite unit 2: (a) Lenticular lithic-rich facies interlayered within the massive  
941 ignimbrite, (b) detail of lenticular lithic-rich facies; note the subangular fragments; (c, d) Ignimbrite  
942 unit 3: (c) massive lithic breccia facies, (d) general view of the massive ignimbrite facies with  
943 columnar jointing at medial facies.

944

945 Fig. 7. Ignimbrite unit 4. (a) Detail of fine-grained cross-stratified facies, (b) detail of fine-grained  
946 planar-stratified facies with levels of concentration of pumices, (c) intercalated sets of fine-grained  
947 cross-stratified and massive ignimbrite facies, (d) detail of pumice-rich facies with dark colours due to  
948 preferential alteration, (e) columnar jointing in welded ignimbrites near the southern rim of the  
949 caldera; note the deformation in the upper portions, (f) pumice-rich massive ignimbrite facies with  
950 blocks of dacitic ignimbrite indicated by an arrow, (g) detail of pumice-rich massive ignimbrite, (h)  
951 massive lithic breccia facies with blocks of dacitic ignimbrite.

952

953 Fig. 8. Sedimentation rate as a function of the  $T_{dep}/T_g$  ratio calculated for different shear zone  
954 thicknesses (1–2 m) and for different large eruption durations (5–50 h). The grey area represents the  
955 thermo-mechanical conditions in which ductile deformation is possible within the aggrading deposit.

956

957 Fig. 9. Schematic reconstruction of facies architecture of the Coranzulí ignimbrites derived from facies  
958 relations from stratigraphic logs of this work and from Seggiaro et al. (2019). General views in (a)

959 northern, (b) eastern, (c) north-western and (d) southern directions from the caldera. These cartoons  
960 are not to scale.

961

962 **Table captions:**

963 Table 1. Field data corresponding to the local deposit thickness,  $h$ , and the application of the model to  
964 calculate ranges of the accumulation rate,  $A_r$ , emplacement timescale,  $t$ , and accumulation velocity,  
965  $h/t$ ; \* no log is available for this point, only its thickness at the locations shown in Fig. 2.

## Highlights

- Coranzulí caldera generated four ignimbrite units at 6.6 Ma
- A theoretical model of emplacement dynamics was developed
- Dense PDCs were subject to rapid *en masse* emplacement
- Emplacement was influenced by paleotopography only locally
- PDCs travelled at relatively low velocities (less than tens of m/s)

Figure 1  
[Click here to download high resolution image](#)

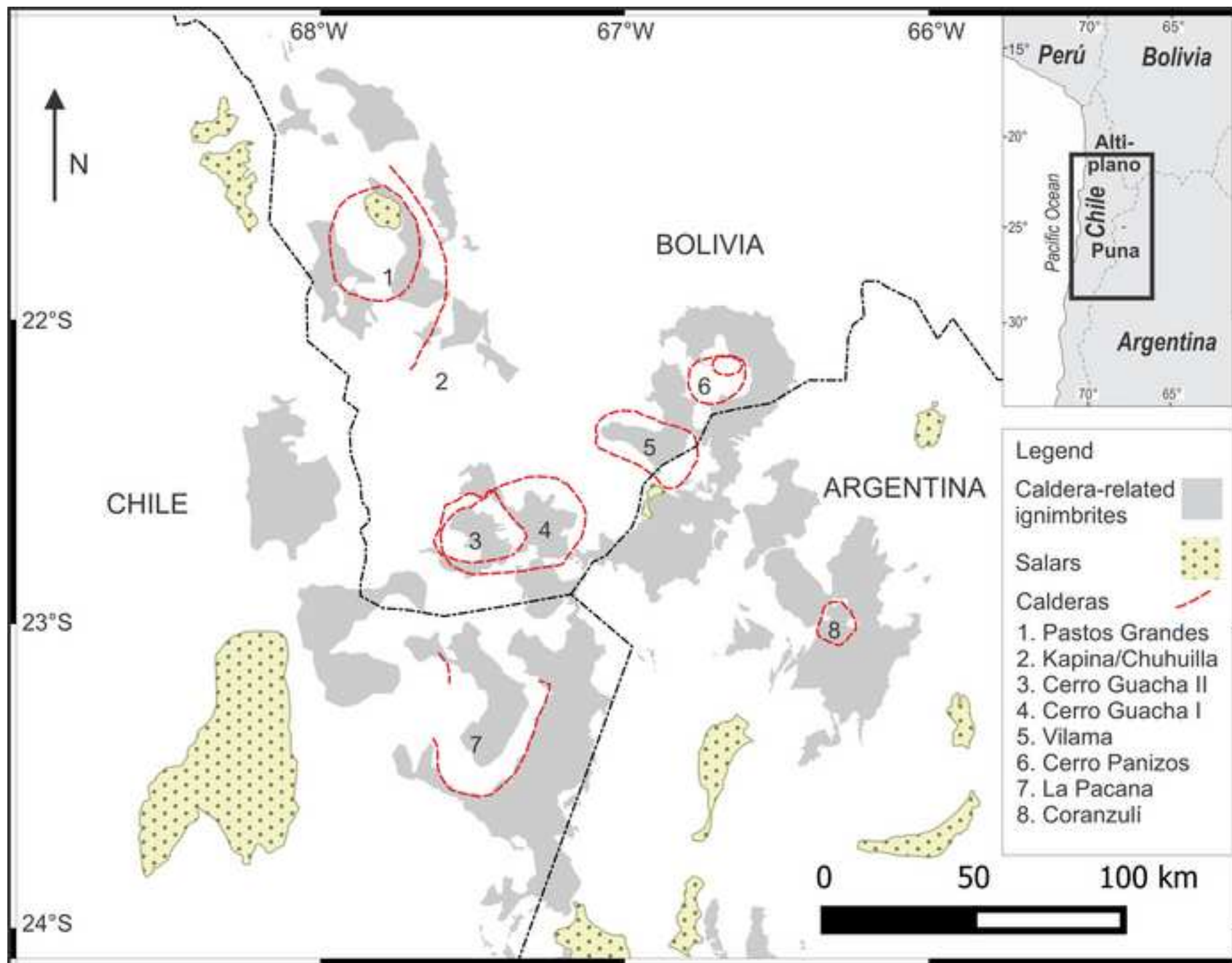
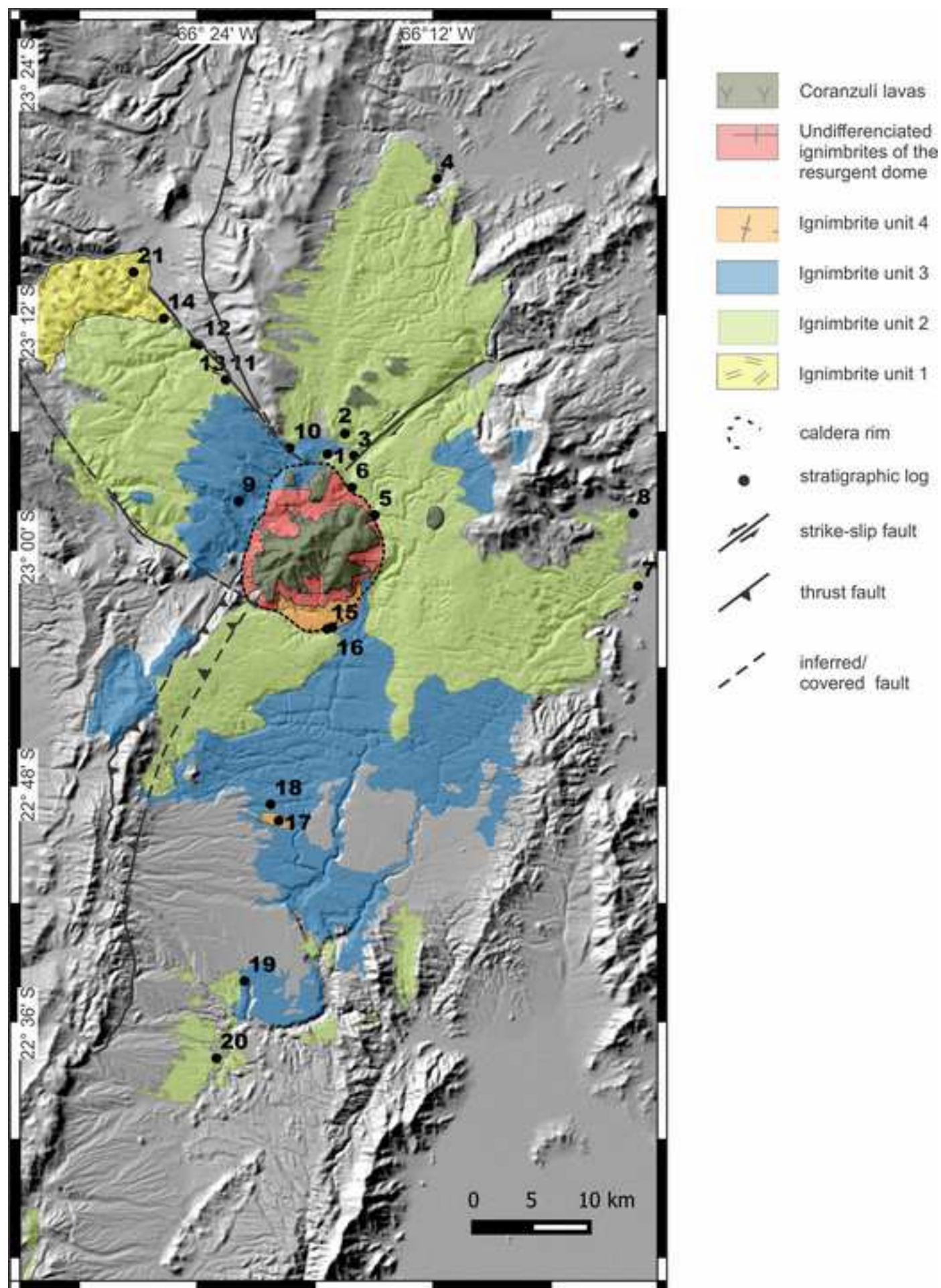


Figure 2

[Click here to download high resolution image](#)



**Figure 3d**  
[Click here to download high resolution image](#)

Profiles to the south of Coranzuli caldera

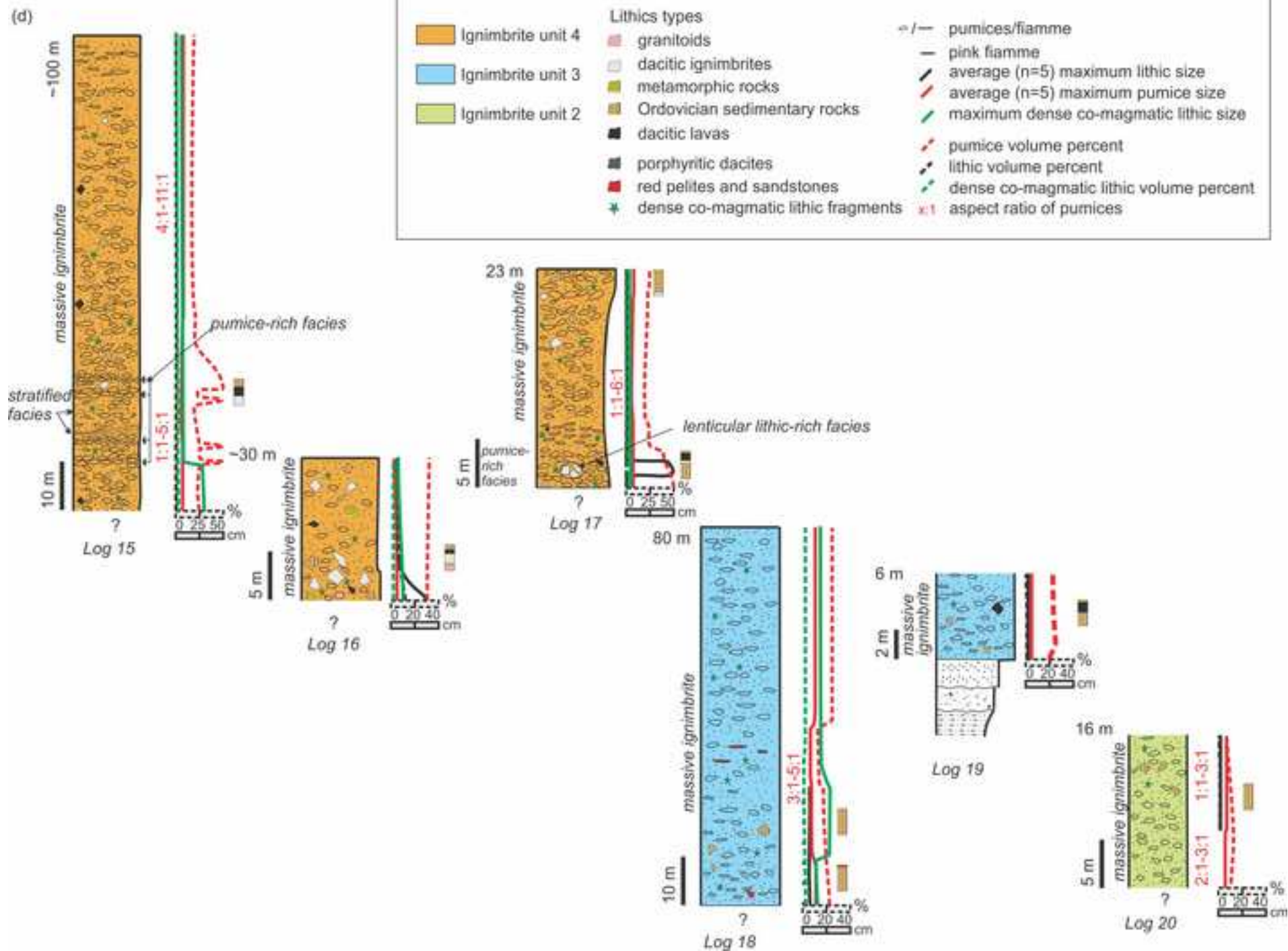


Figure 3b  
[Click here to download high resolution image](#)

Profiles to the east of Coranzuli caldera

(b) 200 m

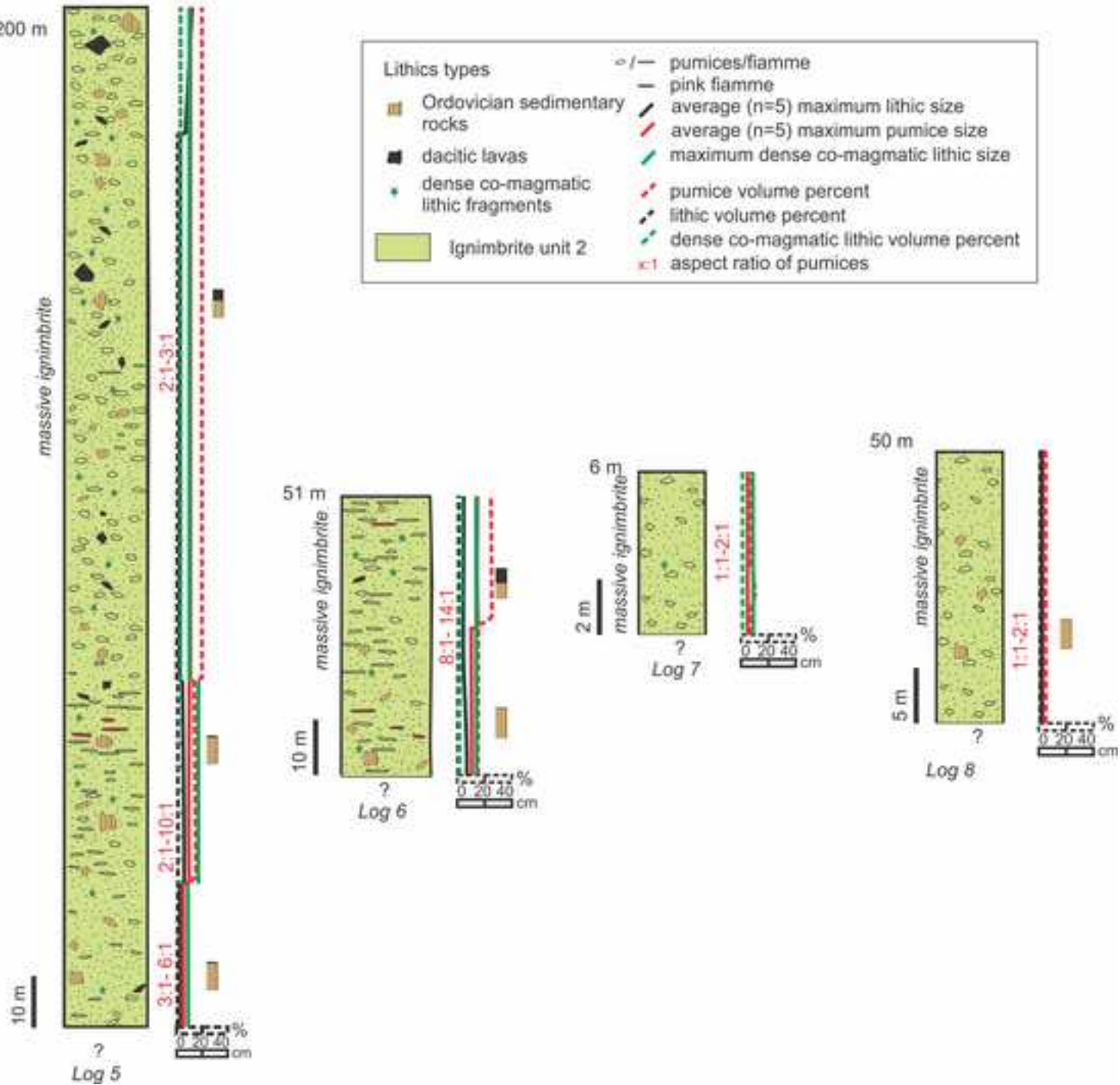


Figure 4

[Click here to download high resolution image](#)



**Figure 3c**  
[Click here to download high resolution image](#)

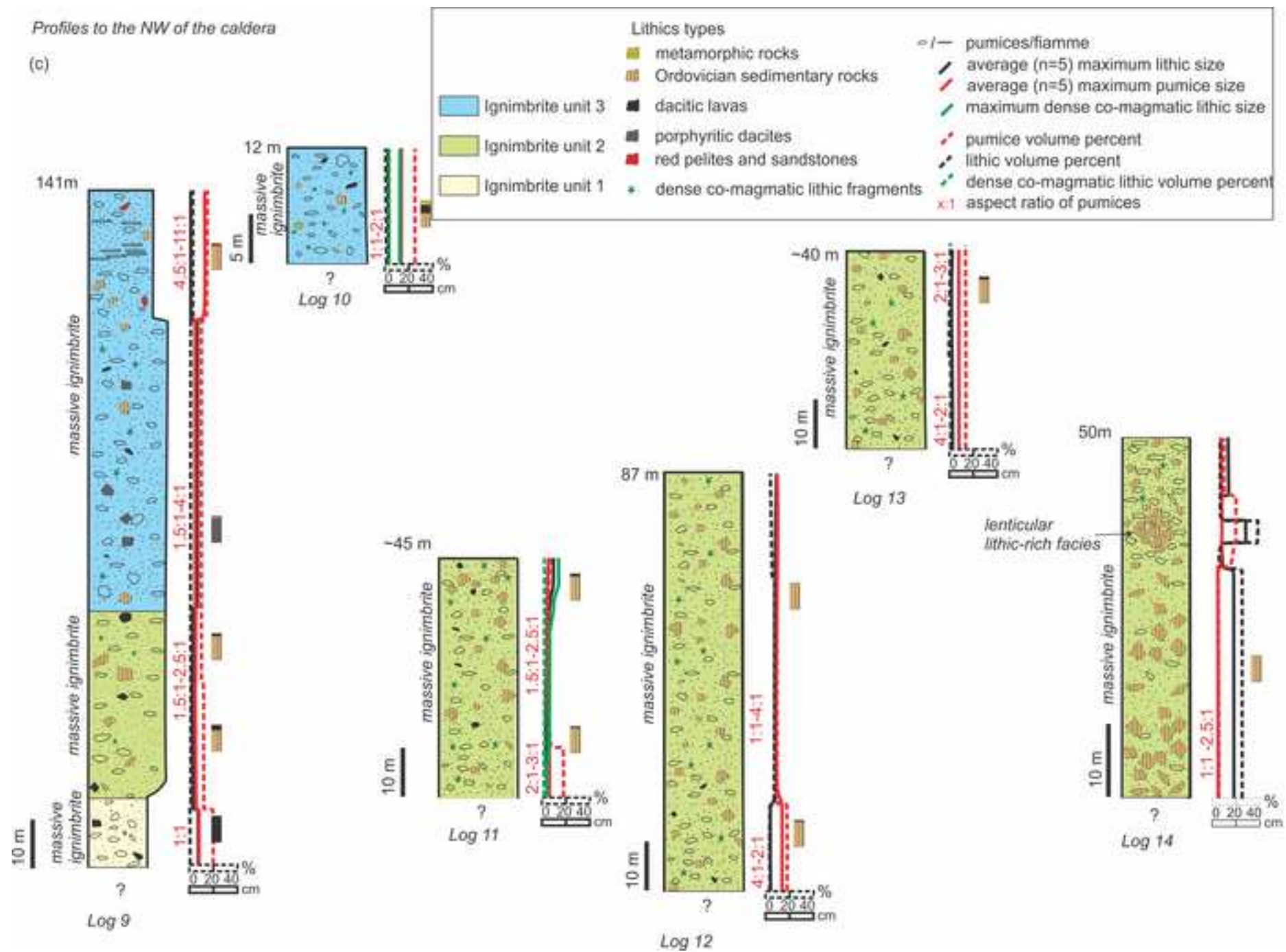
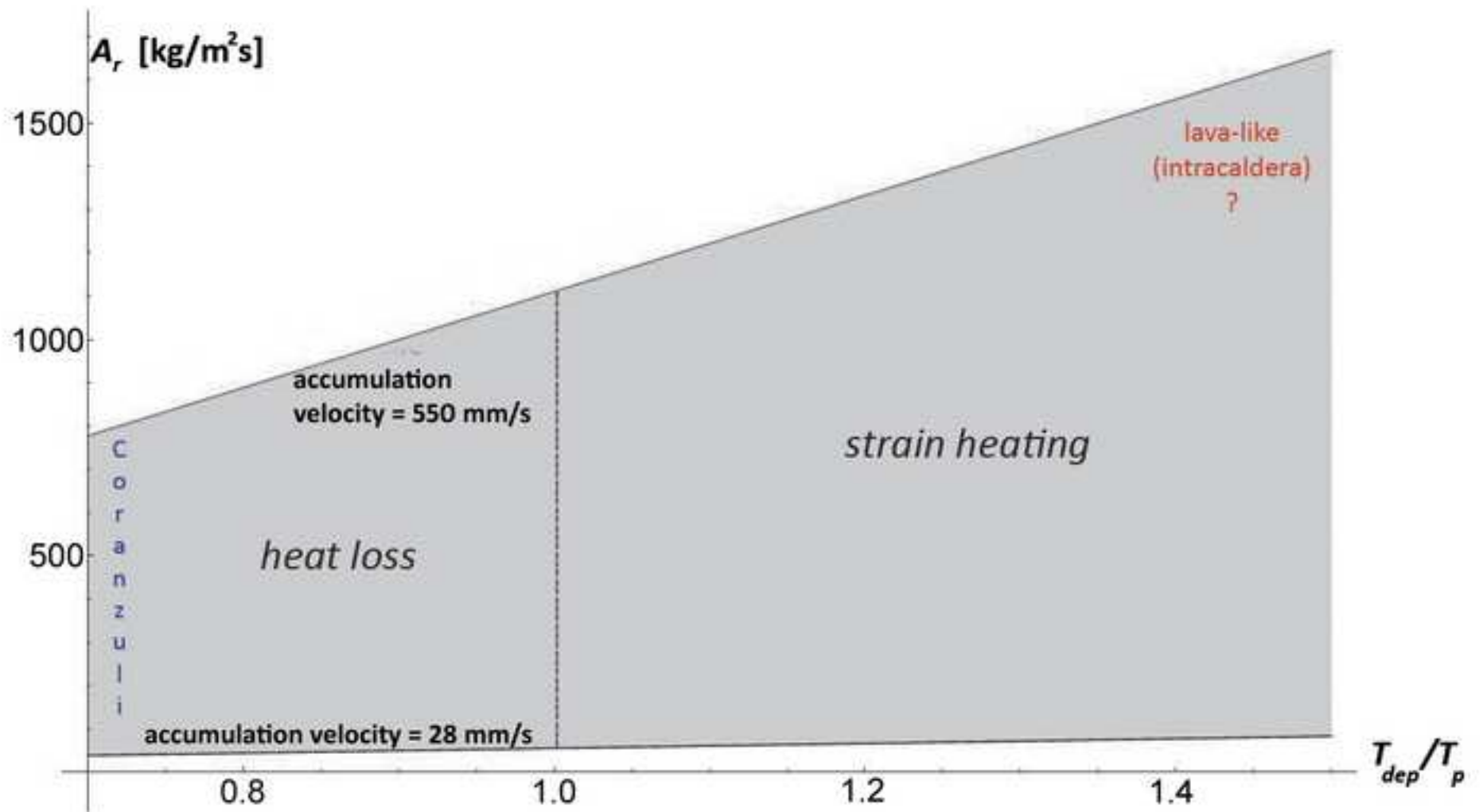


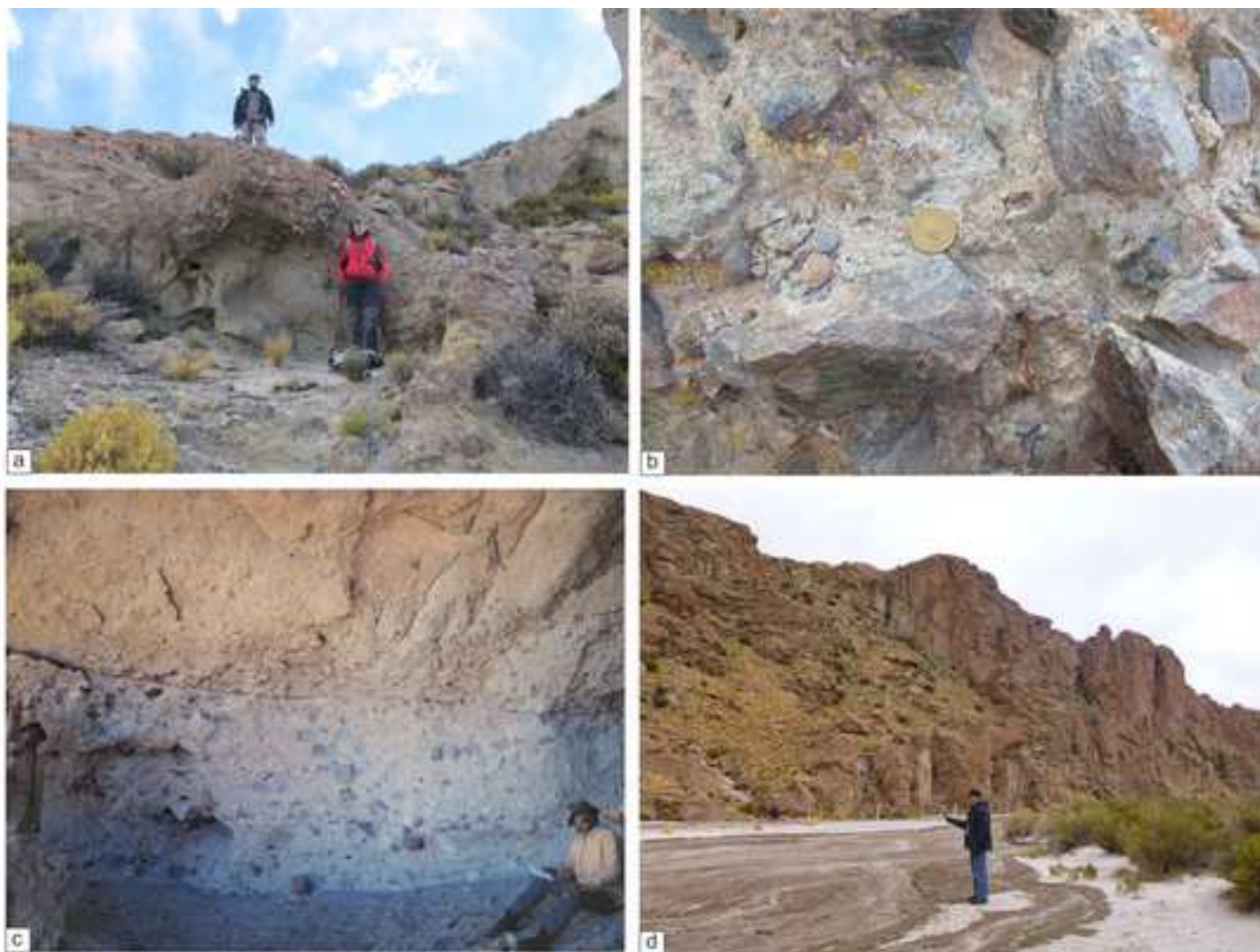
Figure 5  
[Click here to download high resolution image](#)



Figure 8  
[Click here to download high resolution image](#)



**Figure 6**  
[Click here to download high resolution image](#)



**Figure 3a**  
[Click here to download high resolution image](#)

Profiles to the north of Coranzuli caldera

(a)

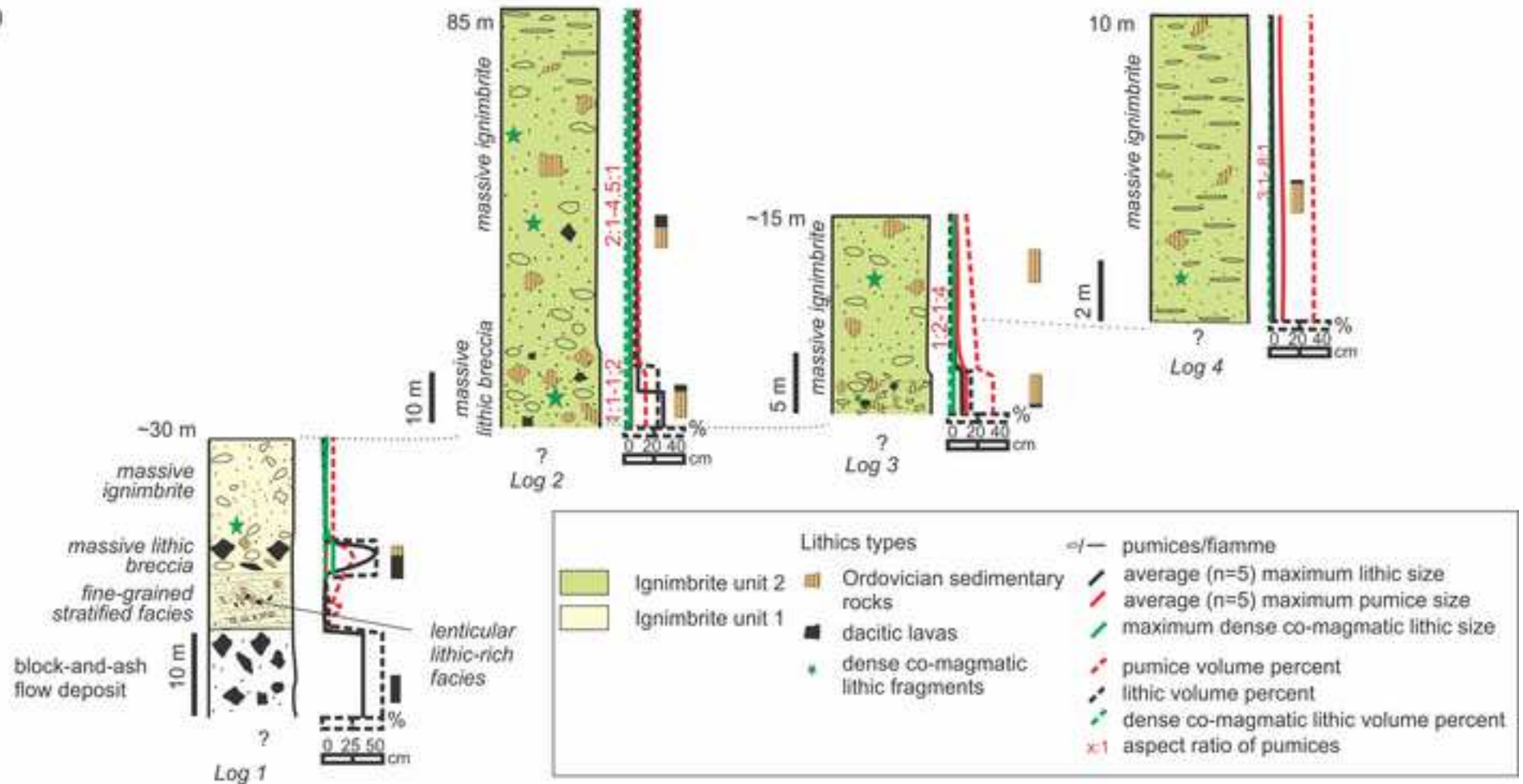


Figure 7

[Click here to download high resolution image](#)



# 1 **Characteristics and emplacement mechanisms of the Coranzulí ignimbrites (Central Andes)**

2 Silvina Guzmán<sup>a,\*</sup>, Domenico M. Doronzo<sup>b</sup>, Joan Martí<sup>b</sup>, Raúl Seggiaro<sup>a</sup>

3

4 <sup>a</sup> Instituto de Bio y Geociencias del NOA (IBIGEO), UNSa, CONICET, 9 de Julio 14, 4405, Rosario  
5 de Lerma, Salta, Argentina.

6 <sup>b</sup> Instituto de Ciencias de la Tierra Jaume Almera, ICTJA-CSIC, Lluís Solé i Sabarís s/n, 08028,  
7 Barcelona, Spain.

8 \* Corresponding author: [sguzman@conicet.gov.ar](mailto:sguzman@conicet.gov.ar)

## 9 **Abstract**

10

11 We present a detailed stratigraphy of the Coranzulí caldera-forming deposits. This caldera, located in  
12 the Altiplano-Puna Volcanic Complex (Central Andes), generated four ignimbrite deposits with  
13 similar field characteristics and facies that differ from each other in, above all, the nature of the lithic  
14 fragments they contain. Three different lithofacies (fine-grained cross-stratified facies, massive lithic  
15 breccia facies and massive ignimbrite facies) are found in all the ignimbrite deposits, which  
16 occasionally also contain a lenticular lithic-rich facies and/or a pumice-rich facies. These field  
17 characteristics and, in particular, local deposit thicknesses were used to develop a theoretical model of  
18 the dynamics and emplacement mode of the Coranzulí pyroclastic flows. Our results show that these  
19 ignimbrites were emplaced by dense pyroclastic density currents subjected to high accumulation rates  
20 and velocities, thereby indicating rapid *en masse* emplacement that was also influenced by local  
21 paleotopography as deduced from facies analysis.

22

23 **Keywords:** Coranzulí; Central Andes; Puna; crystal-rich ignimbrites; pyroclastic density current;  
24 Altiplano-Puna Volcanic Complex

25

## 26 **1. Introduction**

27 In the Altiplano-Puna Volcanic Complex (APVC; de Silva, 1989) within the Altiplano-Puna  
28 plateau large-volume explosive volcanism took place just prior to the late Miocene (Fig. 1). The

**Figure 9**  
[Click here to download high resolution image](#)

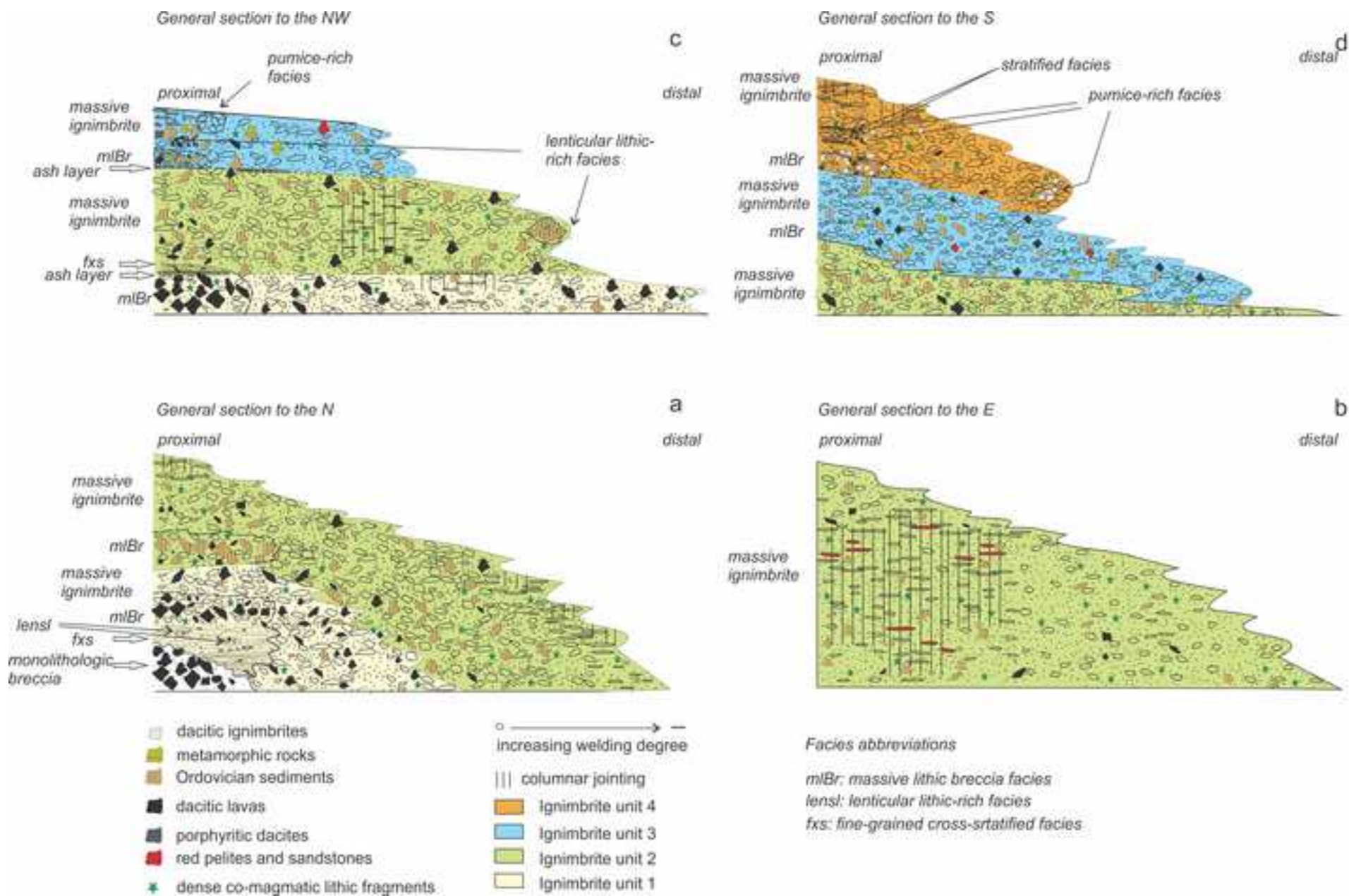


**Table 1**[Click here to download Table: Table 1.doc](#)

---

<i>Profile</i> (Figs.2, 3)	<i>h</i> [m]	<i>A<sub>r</sub></i> min-max [kg/m <sup>2</sup> s]	<i>t</i> min-max [min]	<i>h/t</i> min-max [mm/s]
21*	12	0.6 - 11.2	25.0 - 500.0	0.4 - 8.0
17	23	2.1 - 41.1	13.0 - 260.9	1.5 - 29.4
18	80	24.9 - 497.8	3.7 - 75.0	17.8 - 355.6
20	16	1.0 - 19.9	18.7 - 375.0	0.7 - 14.2
7	6	0.1 - 2.8	50.0 - 1000.0	0.1 - 2.0
8	50	9.7 - 194.4	6.0 - 120.0	6.9 - 138.9
2	85	28.1 - 561.9	3.5 - 70.6	20.1 - 401.4
5	200	155.5 - 3111.1	1.5 - 30.0	111.1 - 2222.2
12	87	29.4 - 588.7	3.4 - 69.0	21.0 - 420.5
14	50	9.7 - 194.4	6.0 - 120.0	6.9 - 138.9
6	51	10.1 - 202.3	5.9 - 117.6	7.2 - 144.5
10	12	0.6 - 11.2	25.0 - 500.0	0.4 - 8.0
4	10	0.4 - 7.8	30.0 - 600.0	0.3 - 5.6
9	141	77.3 - 1546.3	2.1 - 42.5	55.2 - 1104.5

---

**Table 1**